Fourier transform approach to nonperiodic boundary value problems in porous conductive media

Quy-dong To, Guy Bonnet, Trung Nguyen-Thoi

Fourier transform approach to nonperiodic boundary value problems in porous conductive media

Quy-Dong To[1,2,3] | **Guy Bonnet**[3] | **Trung Nguyen-Thoi**[1,2]

[1]Division of Construction Computation, Institute for Computational Science, Ton Duc Thang University, Ho Chi Minh City, Vietnam

[2]Faculty of Civil Engineering, Ton Duc Thang University, Ho Chi Minh City, Vietnam

[3]Laboratoire MSME, Universite Gustave Eiffel, Marne la Vallee, France

Correspondence
Quy-Dong To, Division of Construction Computation, Institute for Computational Science, Ton Duc Thang University, Ho Chi Minh City, Vietnam.
Email: toquydong@tdtu.edu.vn

Abstract

In this article, we develop an extension of the Fourier transform solution method in order to solve conduction equation with nonperiodic boundary conditions (BC). The periodic Lippmann–Schwinger equation for porous materials is extended to the case of non-periodicity with relevant source terms on the boundary. The method is formulated in Fourier space based on the temperature as unknown, using the exact periodic Green function and form factors to describe the boundaries. Different types of BC: flux, temperature, mixed and combined with periodicity can be treated by the method. Numerical simulations show that the method does not encounter convergence issues due to the infinite contrast and yields accurate results for both local fields and effective conductivity.

KEYWORDS

Fourier transform, nonperiodic problems, numerical homogenization

1 | INTRODUCTION

In the determination of effective properties like in micromechanics, Fourier transform is a robust numerical method to solve the local periodic problems and computes the effective properties of the heterogeneous materials from the constituents. Based on the Green tensors, the Lippmann–Schwinger (LS) type equations[1,2] can be formulated and iterative schemes can be used to obtain solutions. The periodicity of the problem is also compatible with fast Fourier transform (FFT) algorithm which proves to be very efficient in this case.

Since the first papers,[3,4] advances have been made in this field. In addition to linear elasticity and conduction problems, the method was extended to a large range of engineering applications like fluid flows,[5] nonlinear behavior,[6,7] finite strain,[8] and so forth. Investigating the properties of the LS equations and improving the convergence of the iteration schemes are the focuses of numerous works. Accelerated scheme can be derived from polarization basis,[9,10] leading to reduced spectral radius and increasing significantly the convergence rate. From the variational principle, the linear equation of polarization can be obtained at stationary state and solved using the conjugate gradient techniques.[11] The original Moulinec–Suquet setting corresponds to Galerkin discretization in trigonometric polynomials space[12,13] and the resolution schemes can be implemented in couple with Newton–Krylov solvers, including conjugate gradient method.[14-17] Willot et al.[18] used a modified discrete Green tensor and obtained convergence with the method, even in the case of infinite contrast limits. Moulinec and Silva[19] discussed the paper in comparison with earlier works on the FFT method and emphasized the importance of the convergence criteria to terminate the iteration scheme. They also showed that the most demanding criteria, expressing energy conservation and compatibility, cannot be achieved at the same time at the infinite contrast by mostly used schemes. Schneider et al.[20] argued that using flux divergence criteria could result in a very slow convergence and proposed a less severe criteria to stop the iterations.

The special cases where the local conductivity can be zero (pore) or infinite (superconductive) are called infinite contrast. In those cases, there exists an eigenvalue of the iteration operator equal to 1 which is responsible for the convergence issues of the iterative schemes. Some numerical schemes seem to provide convergence in the case of infinite contrast, but the theoretical estimation of the eigenvalues related to these schemes cannot achieve to prove the convergence. To and Bonnet[21] realized that the unit eigenvalue is associated to the nonuniqueness of the solution within the pores and provided a solution excluding the fields in the pore in the formulation. In the context of porous conductive materials, a LS equation was derived with the temperature in the skeleton phase as unknown. The associated iterative scheme converges fast and yields accurate local fields.

The FFT method is mainly used in order to provide the effective properties of periodic heterogeneous media. However, considering the benefits of FFT method, one can question if the method can be used also to solve classical boundary value problems with Dirichlet or Neumann boundary conditions (BC) at the boundary of a closed domain. These problems have been addressed recently[22,23] using modified discrete Green tensors. Different from the classical Green tensor obtained by the Fourier transform of the Laplace equation, the discrete counterpart is issued from the finite difference approximation and achieved the convergence even for the infinite contrast limits.[18] It was shown recently that the problem of porous media can be solved using the original Green function[21] and the form factor of boundaries in Fourier space. It is suggested that the same method can be extended to general boundary values problems.

Therefore, in the present article, we consider nonperiodic problems in the determination of effective conduction of porous media. By investigating the periodic conduction equation with source term, we show that the LS equation based on the continuous Green function for periodic porous media equations can tackle nonperiodic BC: flux, temperature, and mixed BC, with or without periodicity in one or two directions. This article is organized as follows. After the "Introduction" section, Section 2 is devoted to theoretical formulation. We revisit the periodic conduction equation with source term and the associated LS equations. The extension to problems with flux and temperature BC in homogenization is also presented. We present numerical tests of the new iterative schemes in Section 3 and discuss the results before concluding in Section 4.

2 | PROBLEM FORMULATION

2.1 | Fourier transform and notations

In what follows, we shall use bold characters to represent tensors and vectors $\boldsymbol{u}$ and normal characters for scalars u. By writing two quantities next to each other, we imply simple product $\varphi\boldsymbol{u}$ (between a scalar and a tensor) or contracted product $\boldsymbol{uv}$ (between a tensor and another tensor). The notation $*$ is used for convolution product, which will be explained later.

For a V periodic function $\boldsymbol{u}(\boldsymbol{x})$ of real variable $\boldsymbol{x}(x_1, x_2, x_3)$, its Fourier transform is denoted as $\boldsymbol{u}(\boldsymbol{\xi})$, function of wave vector $\boldsymbol{\xi}(\xi_1, \xi_2, \xi_3)$

$$\boldsymbol{u}(\boldsymbol{\xi}) = \frac{1}{V}\int_V \boldsymbol{u}(\boldsymbol{x}) e^{-i\boldsymbol{\xi}\cdot\boldsymbol{x}} d\boldsymbol{x}, \quad i = \sqrt{-1} \tag{1}$$

and

$$\xi_k = 2\pi n_k / L_k, \quad n_k = 0, \pm 1, \pm 2, \ldots, \pm\infty, \quad k = 1, 2, 3 \tag{2}$$

Here L_1, L_2, L_3 are dimensions of V in the cartesian coordinate system. The convolution products $\boldsymbol{u}(\boldsymbol{x}) * \boldsymbol{v}(\boldsymbol{x})$ in the real space and $\boldsymbol{u}(\boldsymbol{\xi}) * \boldsymbol{v}(\boldsymbol{\xi})$ in the Fourier space are defined as

$$(\boldsymbol{u} * \boldsymbol{v})(\boldsymbol{x}) = \sum_{\xi} \boldsymbol{u}(\boldsymbol{\xi})\boldsymbol{v}(\boldsymbol{\xi}) e^{i\boldsymbol{\xi}\boldsymbol{x}}, \quad (\boldsymbol{u} * \boldsymbol{v})(\boldsymbol{\xi}) = \sum_{\xi'} \boldsymbol{u}(\boldsymbol{\xi} - \boldsymbol{\xi}')\boldsymbol{v}(\boldsymbol{\xi}') \tag{3}$$

In this article, we use a set of operators $\boldsymbol{P}$, $\boldsymbol{Q}$, $\boldsymbol{H}$, $\boldsymbol{R}$, and S whose expressions in the Fourier space $\boldsymbol{P}(\boldsymbol{\xi})$, $\boldsymbol{Q}(\boldsymbol{\xi})$, $\boldsymbol{H}(\boldsymbol{\xi})$, $\boldsymbol{R}(\boldsymbol{\xi})$, and $S(\boldsymbol{\xi})$ are explicit functions of wavevector $\boldsymbol{\xi}$, given for $\boldsymbol{\xi} \neq \boldsymbol{0}$ by

$$\begin{aligned} &\boldsymbol{P}(\boldsymbol{\xi}) = \overline{\boldsymbol{\xi}} \otimes \overline{\boldsymbol{\xi}}, \quad \boldsymbol{Q}(\boldsymbol{\xi}) = \boldsymbol{I} - \boldsymbol{P}(\boldsymbol{\xi}), \quad \boldsymbol{H}(\boldsymbol{\xi}) = \boldsymbol{Q}(\boldsymbol{\xi}) - \boldsymbol{P}(\boldsymbol{\xi}) \\ &S(\boldsymbol{\xi}) = 1/\xi^2, \quad \boldsymbol{R}(\boldsymbol{\xi}) = \frac{i\boldsymbol{\xi}}{\xi^2}, \quad \forall \boldsymbol{\xi} \neq \boldsymbol{0} \end{aligned} \tag{4}$$

and null for $\boldsymbol{\xi} = \mathbf{0}$

$$\boldsymbol{P}(\mathbf{0}) = \boldsymbol{Q}(\mathbf{0}) = \boldsymbol{H}(\mathbf{0}) = \mathbf{0}, \quad R(\mathbf{0}) = \mathbf{0}, \quad S(\mathbf{0}) = 0 \tag{5}$$

Here, $\boldsymbol{I}$ is the identity tensor and $\overline{\boldsymbol{\xi}}$ the wave vector direction $\overline{\boldsymbol{\xi}} = \boldsymbol{\xi}/\xi$, $\xi = |\boldsymbol{\xi}|$. We also note the following property of operator $\boldsymbol{R}$

$$-\boldsymbol{R} * \nabla\varphi = \varphi - \langle\varphi\rangle \tag{6}$$

for any function φ with $\langle\varphi\rangle$ being the average of φ. This can be proved by taking the Fourier transform of both sides of (6) and considering the expression of $\boldsymbol{R}$ in (4).

2.2 | Periodic LS equations with source term

Let us consider a heterogeneous material where the local conductivity $k(\boldsymbol{x})$ is a periodic function of the coordinate $\boldsymbol{x}$ with period V of dimensions $V = L_1 \times L_2 \times L_3$ in the Cartesian coordinate system. The governing equations of the problem are the following

$$\boldsymbol{e}(\boldsymbol{x}) = \boldsymbol{E} + \nabla\theta(\boldsymbol{x}), \quad \operatorname{div}\boldsymbol{j}(\boldsymbol{x}) + s(\boldsymbol{x}) = 0, \quad \boldsymbol{j}(\boldsymbol{x}) = k(\boldsymbol{x})\boldsymbol{e}(\boldsymbol{x}) \tag{7}$$

where θ, $\boldsymbol{e}$, $\boldsymbol{j}$, and s are the V periodic temperature, (minus) temperature gradient, heat flux, and source term with volume averages Θ, $\boldsymbol{E}$, $\boldsymbol{J}$, and 0

$$\langle\theta(\boldsymbol{x})\rangle = \Theta, \quad \langle\boldsymbol{e}(\boldsymbol{x})\rangle = \boldsymbol{E}, \quad \langle\boldsymbol{j}(\boldsymbol{x})\rangle = \boldsymbol{J}, \quad \langle s(\boldsymbol{x})\rangle = 0 \tag{8}$$

The last condition $\langle s(\boldsymbol{x})\rangle = 0$ is necessary for the existence of a periodic flux $\boldsymbol{j}$. The temperature function θ is the periodic part of the real temperature T which is not necessarily periodic. The relation between T and θ is

$$T(\boldsymbol{x}) = -\theta - \boldsymbol{E}\boldsymbol{x} \tag{9}$$

and only in the case where $\boldsymbol{E} = \mathbf{0}$, T is periodic and identical to θ.

Due to the periodicity, the problem can be solved using Fourier series. Writing the first two equations of (7) in Fourier space yields

$$i\boldsymbol{\xi} \times \boldsymbol{e}(\boldsymbol{\xi}) = \mathbf{0}, \quad i\boldsymbol{\xi}.[\boldsymbol{j}(\boldsymbol{\xi}) - \boldsymbol{R}(\boldsymbol{\xi})s(\boldsymbol{\xi})] = 0 \tag{10}$$

where $\boldsymbol{e}$ is rotation free and $\boldsymbol{j} - \boldsymbol{R} * s$ is divergence free.

Taking an arbitrary reference conductivity k_0, the heterogeneity effects $(k(\boldsymbol{x}) - k_0)\boldsymbol{e}$ and the source term $-\boldsymbol{R} * s$ can be viewed as polarization terms. As a result, one can write

$$\boldsymbol{e}(\boldsymbol{x}) = \boldsymbol{E} - \frac{1}{k_0}\boldsymbol{P} * (\delta k\boldsymbol{e} - \boldsymbol{R} * s), \quad \delta k(\boldsymbol{x}) = k(\boldsymbol{x}) - k_0 \tag{11}$$

or equivalently, due to the properties of $\boldsymbol{R}$ and $\boldsymbol{P}$

$$\boldsymbol{e}(\boldsymbol{x}) = \boldsymbol{E} + \frac{1}{k_0}\boldsymbol{R} * s - \boldsymbol{P} * \left[(\delta k/k_0)\boldsymbol{e}\right] \tag{12}$$

which is an equation with $\boldsymbol{e}$ as unknown to be solved.

In analogous manner, we can also establish an integral equation for $\boldsymbol{j}$ in real space as follows

$$\boldsymbol{j}(\boldsymbol{x}) = \boldsymbol{J} + \boldsymbol{R} * s + \boldsymbol{Q} * \left[(\delta k/k)\boldsymbol{j}\right] \tag{13}$$

Finally, by posing the polarization quantities $\boldsymbol{\tau}$

$$\boldsymbol{\tau}(\boldsymbol{x}) = (k(\boldsymbol{x}) + k_0)\boldsymbol{e}(\boldsymbol{x}), \quad \langle \boldsymbol{\tau}(\boldsymbol{x}) \rangle = \boldsymbol{T} = \boldsymbol{J} + k_0 \boldsymbol{E} \tag{14}$$

we can derive a corresponding equation for $\boldsymbol{\tau}$

$$\boldsymbol{\tau}(\boldsymbol{x}) = \boldsymbol{T} + 2\boldsymbol{R} * s + \boldsymbol{H} * \left[\frac{k - k_0}{k + k_0} \boldsymbol{\tau} \right] \tag{15}$$

To solve problem (7) with known source term s and three average quantities $\boldsymbol{E}$ or $\boldsymbol{J}$ or $\boldsymbol{T}$, we can make use of the linearity by solving two separate problems and then superposing the solutions. The first is a traditional homogenization problem with $s = 0$ and $\boldsymbol{E} \neq 0$ (and $\boldsymbol{J} \neq 0$, $\boldsymbol{T} \neq 0$) and the second only involves the source term $s \neq 0$ and $\boldsymbol{E} = \boldsymbol{J} = \boldsymbol{T} = 0$. We can choose either of the three governing equations (12), (13), and (15) using standard iteration schemes: $\boldsymbol{e}$ (gradient), $\boldsymbol{j}$ (flux), $\boldsymbol{\tau}$ (polarization or accelerated) schemes. The common points of those equations are that they have the form

$$\boldsymbol{u}(\boldsymbol{x}) = \boldsymbol{A} + \boldsymbol{B} * (\epsilon \boldsymbol{u}) \tag{16}$$

where $\boldsymbol{A}$ and ϵ are known functions, $\boldsymbol{B} *$ is an operator with an explicit expression in Fourier space, and $\boldsymbol{u}$ (which can be either $\boldsymbol{e}$ or $\boldsymbol{j}$ or $\boldsymbol{\tau}$) represents the unknown to be obtained (see Table 1). The equation can be solved by iteration described in Algorithm 1 where $\boldsymbol{u}^{(n)}$, $\boldsymbol{u}^{(n+1)}$ are values of two consecutive steps n, $n+1$, leading to the final Neumann series solution

$$\lim_{n \to \infty} \boldsymbol{u}^{(n)}(\boldsymbol{x}) = \sum_{n=0}^{\infty} (\boldsymbol{B} * \epsilon)^n \boldsymbol{A} \tag{17}$$

At each step n, the gradient $\boldsymbol{e}^{(n)}$ and the heat flux $\boldsymbol{j}^{(n)}$ will be computed from $\boldsymbol{u}^{(n)}$ using the constitutive equations. The convergence criteria based on (10) will be used to stop the iterations, specifically the $\boldsymbol{e}$ criteria

$$\| i\boldsymbol{\xi} \times \boldsymbol{e}^{(n)}(\boldsymbol{\xi}) \|_F < \varepsilon \tag{18}$$

and the $\boldsymbol{j}$ criteria

$$\| i\boldsymbol{\xi} . [\boldsymbol{j}^{(n)}(\boldsymbol{\xi}) - \boldsymbol{R}(\boldsymbol{\xi}) s(\boldsymbol{\xi})] \|_F < \varepsilon \tag{19}$$

Here, $\| \|_F$ represents Frobenius norm and ε the smallness factor. Due to the properties of the series as explained in Appendix A, we only need to check $\boldsymbol{j}$ criteria for $\boldsymbol{e}$ scheme, $\boldsymbol{e}$ criteria for $\boldsymbol{j}$ scheme and both $\boldsymbol{j}$ and $\boldsymbol{e}$ criteria for $\boldsymbol{\tau}$ scheme.

Name	$\boldsymbol{u}(\boldsymbol{x})$	$\boldsymbol{A}(\boldsymbol{x})$	$\boldsymbol{B}(\boldsymbol{\xi})$	$\epsilon(\boldsymbol{x})$
$\boldsymbol{e}$ scheme	$\boldsymbol{e}(\boldsymbol{x})$	$\boldsymbol{E} + \frac{1}{k_0}\boldsymbol{R} * s(\boldsymbol{x})$	$-\boldsymbol{P}(\boldsymbol{\xi})$	$\frac{k(\boldsymbol{x}) - k_0}{k_0}$
$\boldsymbol{j}$ scheme	$\boldsymbol{j}(\boldsymbol{x})$	$\boldsymbol{J} + \boldsymbol{R} * s(\boldsymbol{x})$	$\boldsymbol{Q}(\boldsymbol{\xi})$	$\frac{k(\boldsymbol{x}) - k_0}{k(\boldsymbol{x})}$
$\boldsymbol{\tau}$ scheme	$\boldsymbol{\tau}(\boldsymbol{x})$	$\boldsymbol{T} + 2\boldsymbol{R} * s(\boldsymbol{x})$	$\boldsymbol{H}(\boldsymbol{\xi})$	$\frac{k(\boldsymbol{x}) - k_0}{k(\boldsymbol{x}) + k_0}$

TABLE 1 Different iteration schemes with unknown and operators associated to Lippmann–Schwinger equations with source term

Algorithm 1. Schemes for periodic heat transfer problem with source term

Choose a reference conductivity k_0
$\boldsymbol{u}^{(0)}(\boldsymbol{\xi}) = \boldsymbol{A}(\boldsymbol{\xi}), \quad \forall \boldsymbol{\xi}$
Repeat
$\boldsymbol{u}^{(n)}(\boldsymbol{\xi}) = \boldsymbol{A}(\boldsymbol{\xi}) + \boldsymbol{B}(\boldsymbol{\xi})[\epsilon(\boldsymbol{\xi}) * \boldsymbol{u}^{(n-1)}(\boldsymbol{\xi})], \quad \forall \boldsymbol{\xi}$
Compute $\boldsymbol{e}^{(n)}$ and $\boldsymbol{j}^{(n)}$ from $\boldsymbol{u}^{(n)}$ using constitutive equations
$n \leftarrow n + 1$
Until convergence criteria based on $\boldsymbol{e}^{(n)}$ and $\boldsymbol{j}^{(n)}$ satisfied

The convergence of the Neumann series and their corresponding iterative schemes depends on the spectral radii of operators $\boldsymbol{B} * \epsilon$, which are the same as for the normal homogenization problem (i.e., without source term s). They are expected to have the same convergence properties. The three iterative schemes work well when the conductivity $k(\boldsymbol{x})$ is bounded by finite positive values $k_{\min}, k_{\max}$ or $0 < k_{\min} < k(\boldsymbol{x}) < k_{\max} < \infty$. To achieve the optimal convergence, the reference conductivity should be chosen as $k_0 = (k_{\min} + k_{\max})/2$ for $\boldsymbol{e}$ scheme, $k_0 = 2k_{\min}k_{\max}/(k_{\min} + k_{\max})$ for $\boldsymbol{j}$ scheme and $k_0 = \sqrt{k_{\min}k_{\max}}$ for $\boldsymbol{\tau}$ scheme. For infinite contrast cases, that is, $k_{\min} = 0$ or $k_{\max} = \infty$, they cannot guarantee the convergence due to the solution uniqueness issue. In literature, to overcome convergence issues at infinite contrast limits, several researchers[18,23] used the modified Green tensor, which is obtained from finite difference technique, instead of the tensor $\boldsymbol{P}$. However, the theoretical derivation described thereafter will result in a special method for porous material ($k_{\min} = 0$) without changing the nature of the original Green tensor $\boldsymbol{P}$.

2.3 | Temperature scheme for periodic porous materials with source term

Starting from (12) and the relation between θ and $\boldsymbol{e}$, we can derive the following periodic integral equation for θ in V

$$\theta = \Theta + \frac{1}{k_0} S * s + \boldsymbol{R} * \left[(\delta k/k_0)(\nabla\theta + \boldsymbol{E})\right] \tag{20}$$

Now let us consider a porous material where the skeleton is homogeneous with regular conductivity k_r, volume Ω_r (characterized by the indicator function χ_r), and the void occupies volume Ω_v (with the indicator function χ_v), as illustrated in (Figure 1a). Due to the vanishing flux in the pore, the source term s can only be present in the skeleton phase. The conductivity distribution of the whole material reads

$$k(\boldsymbol{x}) = k_r\chi_r(\boldsymbol{x}), \quad \chi_r(\boldsymbol{x}) + \chi_v(\boldsymbol{x}) = 1 \tag{21}$$

The indicator (or characteristic) function χ_α for the phase α ($\alpha = r$ for regular skeleton and $\alpha = v$ for the void phase), behaving like the Heaviside function in 1D, can be defined as

$$\chi_\alpha = 1 \quad \text{in phase } \alpha, \quad \chi_\alpha = 0 \quad \text{in the other phase} \tag{22}$$

We also denote $\boldsymbol{e}_\alpha$ and θ_α the gradient and the temperature restricted to the phase α

$$\boldsymbol{e}_\alpha = \chi_\alpha\boldsymbol{e}, \quad \theta_\alpha = \chi_\alpha\theta, \quad \alpha = r, v \tag{23}$$

We assume that θ_r exists uniquely in the skeleton phase and θ_v is any continuation of θ_r into the void. The strategy is to eliminate θ_v in Equation (20) to derive an equation of θ_r only. By examining the term $\boldsymbol{e}_\alpha = \chi_\alpha(\nabla\theta + \boldsymbol{E})$ in Fourier space, we can show that

$$\begin{aligned}\boldsymbol{e}_\alpha(\boldsymbol{\xi}) &= \boldsymbol{E}\chi_\alpha(\boldsymbol{\xi}) + \frac{1}{V}\int_{\Gamma_\alpha} \theta(\boldsymbol{x})\boldsymbol{n}(\boldsymbol{x})e^{-i\boldsymbol{\xi}\cdot\boldsymbol{x}}ds + i\boldsymbol{\xi}\theta_\alpha(\boldsymbol{\xi}) \\ &= \boldsymbol{E}\chi_\alpha(\boldsymbol{\xi}) + [(\boldsymbol{n}\delta)_{\Gamma_\alpha}\theta](\boldsymbol{\xi}) + i\boldsymbol{\xi}\theta_\alpha(\boldsymbol{\xi})\end{aligned} \tag{24}$$

with $\boldsymbol{n}$ being the outward normal vector of the boundary Γ_α of Ω_α and

$$[(\boldsymbol{n}\delta)_{\Gamma_\alpha}\theta](\boldsymbol{\xi}) = \frac{1}{V}\int_{\Gamma_\alpha} \theta(\boldsymbol{x})\boldsymbol{n}(\boldsymbol{x})e^{-i\boldsymbol{\xi}\cdot\boldsymbol{x}}ds, \tag{25}$$

In this relation, the distribution $(\boldsymbol{n}\delta)_{\Gamma_\alpha}(\boldsymbol{x})$ associated with interface Γ_α is the surface delta distribution δ_{Γ_α} multiplied with the local normal vector $\boldsymbol{n}$. Its Fourier transform expression is

$$(\boldsymbol{n}\delta)_{\Gamma_\alpha}(\boldsymbol{\xi}) = \frac{1}{V}\int_{\Gamma_\alpha} \boldsymbol{n}(\boldsymbol{x})e^{-i\boldsymbol{\xi}\cdot\boldsymbol{x}}ds \tag{26}$$

The determination of $(\boldsymbol{n}\delta)_{\Gamma_\alpha}(\boldsymbol{x})$ for different geometries is presented in Section 2.6.

On the other hand, examining $\boldsymbol{e}_\alpha$ in real space, for example,

$$\boldsymbol{e}_\alpha(\boldsymbol{x}) = \boldsymbol{E}\chi_\alpha(\boldsymbol{x}) + \nabla\theta_\alpha(\boldsymbol{x}) - \theta(\boldsymbol{x})\nabla\chi_\alpha(\boldsymbol{x}) \tag{27}$$

we find that the $(\boldsymbol{n}\delta)_{\Gamma_\alpha}$ distribution is in fact derived from the gradient of the characteristic function χ_α

$$(\boldsymbol{n}\delta)_{\Gamma_\alpha} = -\nabla\chi_\alpha(\boldsymbol{x}) \tag{28}$$

Due to the property of the characteristic function χ_α,[21] we can show that for any continuous function θ (see References 24 and 25 for details on mathematical background of generalized functions)

$$(\nabla\chi_\alpha)(\theta) = 2(\nabla\chi_\alpha)(\chi_\alpha\theta) \quad \text{or} \quad (\boldsymbol{n}\delta)_{\Gamma_\alpha}\theta = 2(\boldsymbol{n}\delta)_{\Gamma_\alpha}\theta_r \tag{29}$$

Following the procedure in Reference 21, we can derive the equation for θ_r only

$$\theta_r = \Theta_r - \boldsymbol{R} * \nabla\theta_r + \frac{1}{k_0}S * s + \frac{k_r}{k_0}\boldsymbol{R} * \boldsymbol{e}_r \tag{30}$$

with

$$\boldsymbol{e}_r = \boldsymbol{E}\chi_r + 2(\boldsymbol{n}\delta)_{\Gamma_r}\theta_r + \nabla\theta_r \tag{31}$$

and Θ_r being the average of θ_r. The numerical schemes associated to (30) with known source term is presented in Algorithm 2. Note that we made use in Reference 21 of the relation

$$\theta_r = \Theta_r - \boldsymbol{R} * \nabla\theta_r \tag{32}$$

to derive the recurrence relation between $\theta_r^{(n+1)}(\boldsymbol{\xi})$ and $\theta_r^{(n)}(\boldsymbol{\xi})$ and showed that the energy conservation condition is also satisfied at convergence.

2.4 | Pure flux BC

Now let us consider a porous material occupying the domain Ω subject to Neumann boundary condition on its boundary. On the external boundary $\partial\Omega$ and internal boundary Γ_r, we apply the flux $\boldsymbol{j}.\boldsymbol{n} = j_n^*$ with $\boldsymbol{n}$ being the outward vector and j_n^* being the known prescribed normal flux. We shall show that this nonperiodic problem can be treated as a particular case of the periodic problem presented in the previous section with suitable continuous extension. In literature, such techniques using the solution of an immersed problem to solve boundary value problems in a domain of arbitrary shape have been employed extensively.[26-29] First, we use a rectangular box V that is large enough to include the domain Ω and consider the solution in Ω as the partial solution of the V periodic problem with a suitable continuation (see Figure 1b).

Algorithm 2. Temperature θ iteration scheme for periodic porous material with source term

Choose a reference conductivity k_0
$\theta_r^{(0)}(\boldsymbol{\xi}) = \frac{1}{k_0}S(\boldsymbol{\xi})s(\boldsymbol{\xi}) + \frac{k_r}{k_0}\boldsymbol{R}(\boldsymbol{\xi})[\boldsymbol{E}\chi_r(\boldsymbol{\xi})], \quad \forall\boldsymbol{\xi}$
Repeat
$\boldsymbol{e}_r^{(n)}(\boldsymbol{\xi}) = \boldsymbol{E}\chi_r(\boldsymbol{\xi}) + i\boldsymbol{\xi}\theta_r^{(n-1)}(\boldsymbol{\xi}) + 2(\boldsymbol{n}\delta)_{\Gamma_r}(\boldsymbol{\xi}) * \theta_r^{(n-1)}(\boldsymbol{\xi}), \quad \forall\boldsymbol{\xi}$
$\boldsymbol{j}^{(n)}(\boldsymbol{\xi}) = k_r\boldsymbol{e}_r^{(n)}(\boldsymbol{\xi}), \quad \forall\boldsymbol{\xi}$
$\theta_r^{(n)}(\boldsymbol{\xi}) = \theta_r^{(n-1)}(\boldsymbol{\xi}) + \frac{1}{k_0}\boldsymbol{R}(\boldsymbol{\xi})\boldsymbol{j}^{(n)}(\boldsymbol{\xi}) + \frac{1}{k_0}S(\boldsymbol{\xi})s(\boldsymbol{\xi}), \quad \forall\boldsymbol{\xi}$
$n \leftarrow n+1$
Until convergence criteria based on $\boldsymbol{j}^{(n)}$ satisfied

In this case, the void filled between V and Ω and the internal void of Ω are treated in the same way. We can choose any continuous temperature field T within the void. The temperature T is also chosen to be periodic so that $\boldsymbol{E} = \boldsymbol{0}$ and $T = -\theta$. We note that there is no source term in our initial problem. However, as we extend the solution domain to the whole domain V, the source term appears due to the discontinuity of the normal heat flux at the boundary $\partial\Omega$ and Γ_r. Outside the domain, $j_n = 0$ and inside it, j_n is equal to the prescribed normal heat flux $j_n = j_n^*$. As a result, those discontinuities are source terms localized on $\partial\Omega$ and Γ_r admitting the Fourier transform

$$s(\boldsymbol{\xi}) = \frac{1}{V}\int_{\partial\Omega\cup\Gamma_r} j_n^*(\boldsymbol{x})e^{-i\boldsymbol{\xi}\cdot\boldsymbol{x}}ds, \quad s(\boldsymbol{0}) = \frac{1}{V}\int_{\partial\Omega\cup\Gamma_r} j_n^*(\boldsymbol{x})ds = 0 \tag{33}$$

In this case, the source term s is known and (30) can be solved by the iteration process described in Algorithm 3. We note that, for the Neumann type problem, the temperature solution can be defined up to a constant. For convenience, we can set the average temperature of the skeleton field $\Theta_r = \langle\theta_r\rangle = 0$. We note that due to the void between Ω and V, the distribution $\boldsymbol{n}\delta$ must be associated to both Γ_r and $\partial\Omega$.

In the case where $\partial\Omega$ is a closed surface on which a homogeneous boundary flux is prescribed,

$$j_n^*(\boldsymbol{x}) = \boldsymbol{G}\boldsymbol{n}(\boldsymbol{x}), \quad \text{on } \partial\Omega \tag{34}$$

with $\boldsymbol{G}$ being a constant vector. This type of BC is frequently used to determine the effective properties of heterogeneous materials and applicable to domains Ω of arbitrary shape. We can write

$$s(\boldsymbol{\xi}) = \frac{\boldsymbol{G}}{V}\int_{\partial\Omega} \boldsymbol{n}(\boldsymbol{x})e^{-i\boldsymbol{\xi}\cdot\boldsymbol{x}}d\boldsymbol{x} = \boldsymbol{G}(\boldsymbol{n}\delta)_{\partial\Omega}(\boldsymbol{\xi}) \tag{35}$$

The explicit expression of $(\boldsymbol{n}\delta)_{\partial\Omega}(\boldsymbol{\xi})$ for different geometries like circles and polylines are given in Section 2.6.

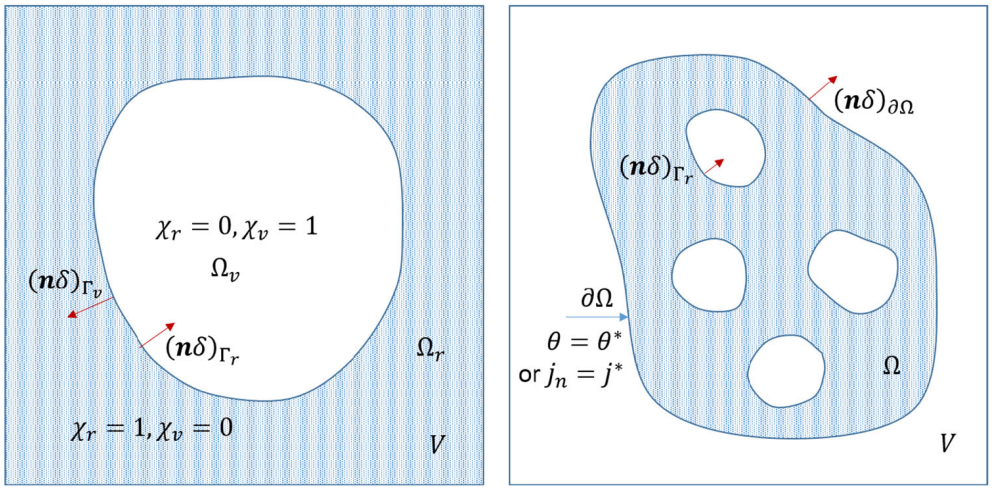

FIGURE 1 Sketch of the periodic (left) and nonperiodic (right) problem

Algorithm 3. Temperature θ iteration scheme for arbitrary porous domain with flux boundary conditions

Choose a reference conductivity k_0
$\theta_r^{(0)}(\boldsymbol{\xi}) = \frac{1}{k_0}S(\boldsymbol{\xi})s(\boldsymbol{\xi}), \quad \forall\boldsymbol{\xi}$
Repeat
$\boldsymbol{e}_r^{(n)}(\boldsymbol{\xi}) = i\boldsymbol{\xi}\theta_r^{(n-1)}(\boldsymbol{\xi}) + 2(\boldsymbol{n}\delta)_{\Gamma_r\cup\partial\Omega}(\boldsymbol{\xi}) * \theta_r^{(n-1)}(\boldsymbol{\xi}), \quad \forall\boldsymbol{\xi}$
$\boldsymbol{j}^{(n)}(\boldsymbol{\xi}) = k_r\boldsymbol{e}_r^{(n)}(\boldsymbol{\xi}), \quad \forall\boldsymbol{\xi}$
$\theta_r^{(n)}(\boldsymbol{\xi}) = \theta_r^{(n-1)}(\boldsymbol{\xi}) + \frac{1}{k_0}\boldsymbol{R}(\boldsymbol{\xi})\boldsymbol{j}^{(n)}(\boldsymbol{\xi}) + \frac{1}{k_0}S(\boldsymbol{\xi})s(\boldsymbol{\xi}), \quad \forall\boldsymbol{\xi}$
$n \leftarrow n + 1$
Until convergence criteria based on $\boldsymbol{j}^{(n)}$ satisfied

To compute the average gradient of the effective porous material, denoted as $\boldsymbol{D}$, we use the distribution of θ on the surface and the average formula

$$\boldsymbol{D} = \frac{1}{\Omega}\int_{\partial\Omega} \theta \boldsymbol{n} d\boldsymbol{x} \tag{36}$$

or equivalently

$$\boldsymbol{D} = \frac{V}{\Omega} 2[(\boldsymbol{n}\delta)_{\partial\Omega}\theta_r](\boldsymbol{\xi} = \boldsymbol{0}) \tag{37}$$

2.5 | Temperature or mixed temperature-flux BC

On part of the boundary, let us say $\partial\Omega^j \cup \Gamma_r^j$, we apply the normal flux as before $j_n = j_n^*$ and on the remaining part $\partial\Omega^t \cup \Gamma_r^t$ we prescribe the temperature $\theta = \theta^*$. However, instead of imposing the temperature θ on $\partial\Omega^t \cup \Gamma_r^t$, we choose to impose its perturbation $\tilde{\theta}$ around its volume average $\overline{\theta}$

$$\tilde{\theta}(\boldsymbol{x}) = \tilde{\theta}^*(\boldsymbol{x}) \quad \text{on} \quad \partial\Omega^t \cup \Gamma_r^t \tag{38}$$

with the definitions

$$\tilde{\theta}(\boldsymbol{x}) = \theta(\boldsymbol{x}) - \overline{\theta}, \quad \tilde{\theta}^*(\boldsymbol{x}) = \theta^*(\boldsymbol{x}) - \overline{\theta}^*, \quad \overline{\theta} = \frac{\int_{\partial\Omega^t \cup \Gamma_r^t} \theta(\boldsymbol{x}) d\boldsymbol{x}}{\int_{\partial\Omega^t \cup \Gamma_r^t} d\boldsymbol{x}}, \quad \overline{\theta}^* = \frac{\int_{\partial\Omega^t \cup \Gamma_r^t} \theta^*(\boldsymbol{x}) d\boldsymbol{x}}{\int_{\partial\Omega^t \cup \Gamma_r^t} d\boldsymbol{x}} \tag{39}$$

As a result, the temperature solution of the above problem is not unique and defined up to a constant which does not affect the gradient and flux fields. To recover the real temperature solution, it is sufficient to take any solution θ of the perturbation prescribed problem and add a constant skeleton field, which is the difference between $\overline{\theta}^*$ and $\overline{\theta}$. The perturbation temperature constraint can be written using the distribution notation

$$t^* - (\delta_{\partial\Omega^t \cup \Gamma_r^t}\theta - \overline{\theta}\delta_{\partial\Omega^t \cup \Gamma_r^t}) = 0, \quad \overline{\theta} = \frac{(\delta_{\partial\Omega^t \cup \Gamma_r^t}\theta)(\boldsymbol{\xi} = \boldsymbol{0})}{(\delta_{\partial\Omega^t \cup \Gamma_r^t})(\boldsymbol{\xi} = \boldsymbol{0})} \tag{40}$$

where t^* is a known distribution

$$t^*(\boldsymbol{\xi}) = \frac{1}{V}\int_{\partial\Omega^t \cup \Gamma_r^t} \tilde{\theta}^*(\boldsymbol{x}) e^{-i\boldsymbol{\xi}.\boldsymbol{x}} ds \tag{41}$$

Like for relation (29), due to the continuity of θ and discontinuity of θ_r on the boundary, we can link the distribution associated to θ with the one associated to θ_r

$$\delta_{\partial\Omega^t \cup \Gamma_r^t}\theta = 2\delta_{\partial\Omega^t \cup \Gamma_r^t}\theta_r \tag{42}$$

and the constraint (40) can be expressed in term of θ_r only.

Regarding the source term s associated to the boundary normal flux j_n, it is known on $\partial\Omega^j \cup \Gamma_r^j$ and unknown on $\partial\Omega^t \cup \Gamma_r^t$. Let us decompose the flux j_n on $\partial\Omega^t \cup \Gamma_r^t$ as sum of the mean value $\bar{j}_n$ and its perturbation $\tilde{j}_n$

$$\tilde{j}_n(\boldsymbol{x}) = j_n(\boldsymbol{x}) - \bar{j}_n, \quad \bar{j}_n = \frac{\int_{\partial\Omega^t \cup \Gamma_r^t} j_n(\boldsymbol{x}) d\boldsymbol{x}}{\int_{\partial\Omega^t \cup \Gamma_r^t} d\boldsymbol{x}} = -\frac{\int_{\partial\Omega^t \cup \Gamma_r^j} j_n^*(\boldsymbol{x}) d\boldsymbol{x}}{\int_{\partial\Omega^t \cup \Gamma_r^t} d\boldsymbol{x}} \tag{43}$$

The last equation of (43) shows that the mean value $\bar{j}_n$ on $\partial\Omega^t \cup \Gamma_r^t$ is known due to the energy conservation, that is, the source distribution s must have zero sum over the periodic cell. We can now write the source term as

$$s(\boldsymbol{\xi}) = \frac{1}{V}\int_{\partial\Omega \cup \Gamma_r} j_n(\boldsymbol{x}) e^{-i\boldsymbol{\xi}.\boldsymbol{x}} ds = s^*(\boldsymbol{\xi}) + \frac{1}{V}\int_{\partial\Omega^t \cup \Gamma_r^t} \tilde{j}_n(\boldsymbol{x}) e^{-i\boldsymbol{\xi}.\boldsymbol{x}} ds \tag{44}$$

with the known source term s^*

$$s^*(\boldsymbol{\xi}) = \frac{1}{V}\int_{\partial\Omega^j\cup\Gamma_r^j} j_n^*(\boldsymbol{x})e^{-i\boldsymbol{\xi}.\boldsymbol{x}}ds + \frac{\bar{j}_n}{V}\int_{\partial\Omega^t\cup\Gamma_r^t} e^{-i\boldsymbol{\xi}.\boldsymbol{x}}ds \tag{45}$$

To impose the perturbation temperature constraint $\tilde{\theta}(\boldsymbol{x}) = \tilde{\theta}^*(\boldsymbol{x})$ in relation to the unknown perturbation normal flux $\tilde{j}_n(\boldsymbol{x})$, a simple method is to use a large interface conductivity coefficient like in the penalty technique. In this case, the normal flux $\tilde{j_n}$ is proportional to the temperature difference $\tilde{\theta}^* - \tilde{\theta}$ on $\partial\Omega^t \cup \Gamma_r^t$

$$\tilde{j_n} = k_{pen}(\tilde{\theta}^* - \tilde{\theta}) \tag{46}$$

with k_{pen} being a sufficiently large penalty coefficient. Including this condition into the source term yield

$$s(\boldsymbol{\xi}) = k_{pen}[t^* - (2\delta_{\partial\Omega^t\cup\Gamma_r^t}\theta_r - \overline{\theta}\delta_{\partial\Omega^t\cup\Gamma_r^t})](\boldsymbol{\xi}) + s^*(\boldsymbol{\xi}) \tag{47}$$

The integral equation for θ_r can be recast into a new abstract form

$$\theta_r = \theta_r + \frac{1}{k_0}S * \left\{k_{pen}[t^* - (2\delta_{\partial\Omega^t\cup\Gamma_r^t}\theta_r - \overline{\theta}\delta_{\partial\Omega^t\cup\Gamma_r^t})] + s^*\right\} + \frac{k_r}{k_0}\boldsymbol{R} * \boldsymbol{e}_r \tag{48}$$

In an alternative way, the constraint can be dealt with the augmented Lagrange method. The multiplier λ is introduced as the unknown source term

$$s = \lambda + s^* \tag{49}$$

to be used in conjunction with the constraint on the temperature

$$\lambda = \lambda + k_L[t^* - (2\delta_{\partial\Omega^t\cup\Gamma_r^t}\theta_r - \overline{\theta}\delta_{\partial\Omega^t\cup\Gamma_r^t})] \tag{50}$$

where the penalty coefficient k_L can be of the same order as the reference conductivity k_0. Numerical experiences have shown that choosing $k_0 = k_{pen}/2$ in the penalty method and $k_0 = 1.2$ and $k_L = k_0$ in the augmented Lagrange method guarantee the best convergence results in terms of number of iterations. After the convergence based on $\boldsymbol{j}$, we also check if the scheme reproduces efficiently the temperature boundary condition by the criteria

$$\frac{\|t^* - (2\delta_{\partial\Omega^t\cup\Gamma_r^t}\theta_r - \overline{\theta}\delta_{\partial\Omega^t\cup\Gamma_r^t})\|_F}{\|\delta_{\partial\Omega^t\cup\Gamma_r^t}\|_F} < \varepsilon \tag{51}$$

Since the solution of the prescribed temperature perturbation problem is defined up to a constant, we set the average temperature in the numerical schemes equal to zero $\Theta_r = \langle\theta_r\rangle = 0$.

Algorithm 4. Temperature θ iteration scheme for arbitrary porous domain with temperature boundary conditions and penalty method

Choose k_{pen} and α and the reference conductivity k_0
$\theta_r^{(0)}(\boldsymbol{\xi}) = 0, \quad \forall\boldsymbol{\xi}$
Repeat
$\boldsymbol{e}_r^{(n)}(\boldsymbol{\xi}) = i\boldsymbol{\xi}\theta_r^{(n-1)}(\boldsymbol{\xi}) + 2(\boldsymbol{n}\delta)_{\partial\Omega\cup\Gamma_r}(\boldsymbol{\xi}) * \theta_r^{(n-1)}(\boldsymbol{\xi}), \quad \forall\boldsymbol{\xi}$
$\boldsymbol{j}^{(n)}(\boldsymbol{\xi}) = k_r\boldsymbol{e}_r^{(n)}(\boldsymbol{\xi}), \quad \forall\boldsymbol{\xi}$
$s^{(n)}(\boldsymbol{\xi}) = s^*(\boldsymbol{\xi}) + k_{pen}[t^* - (2\delta_{\partial\Omega^t\cup\Gamma_r^t}\theta_r - \bar{\theta}\delta_{\partial\Omega^t\cup\Gamma_r^t})](\boldsymbol{\xi})$
$\theta_r^{(n)}(\boldsymbol{\xi}) = \theta_r^{(n-1)}(\boldsymbol{\xi}) + \frac{1}{k_0}\boldsymbol{R}(\boldsymbol{\xi})\boldsymbol{j}^{(n)}(\boldsymbol{\xi}) + \frac{1}{k_0}S(\boldsymbol{\xi})s^{(n)}(\boldsymbol{\xi}), \quad \forall\boldsymbol{\xi}$
$n \leftarrow n + 1$
Until convergence criteria based on $\boldsymbol{j}^{(n)}$ satisfied
Check the boundary conditions on temperature

Algorithm 5. Temperature θ iteration scheme for arbitrary porous domain with temperature boundary conditions and augmented Lagrange method

Choose a reference conductivity k_0, k_L, and α
$\theta_r^{(0)}(\boldsymbol{\xi}) = 0, \quad \lambda^{(0)}(\boldsymbol{\xi}) = 0, \quad \forall \boldsymbol{\xi}$
Repeat
$\boldsymbol{e}_r^{(n)}(\boldsymbol{\xi}) = i\boldsymbol{\xi}\theta_r^{(n-1)}(\boldsymbol{\xi}) + 2(\boldsymbol{n}\delta)_{\partial\Omega\cup\Gamma_r}(\boldsymbol{\xi}) * \theta_r^{(n-1)}(\boldsymbol{\xi}), \quad \forall \boldsymbol{\xi}$
$\boldsymbol{j}^{(n)}(\boldsymbol{\xi}) = k_r\boldsymbol{e}_r^{(n)}(\boldsymbol{\xi}), \quad \forall \boldsymbol{\xi}$
$\lambda^{(n)}(\boldsymbol{\xi}) = \lambda^{(n-1)}(\boldsymbol{\xi}) + k_L[t^* - (2\delta_{\partial\Omega^t\cup\Gamma_r^t}\theta_r - \bar{\theta}\delta_{\partial\Omega^t\cup\Gamma_r^t})](\boldsymbol{\xi})$
$s^{(n)}(\boldsymbol{\xi}) = s^*(\boldsymbol{\xi}) + \lambda^{(n)}(\boldsymbol{\xi})$
$\theta_r^{(n)}(\boldsymbol{\xi}) = \theta_r^{(n-1)}(\boldsymbol{\xi}) + \frac{1}{k_0}\boldsymbol{R}(\boldsymbol{\xi})\boldsymbol{j}^{(n)}(\boldsymbol{\xi}) + \frac{1}{k_0}S(\boldsymbol{\xi})s^{(n)}(\boldsymbol{\xi}), \quad \forall \boldsymbol{\xi}$
$n \leftarrow n+1$
Until convergence criteria based on $\boldsymbol{j}^{(n)}$ satisfied
Check the boundary conditions on temperature

Regarding the homogenization problem in porous material, the following temperature BC are used

$$\theta^*(\boldsymbol{x}) = \boldsymbol{D}\boldsymbol{x}, \quad \text{on } \partial\Omega \tag{52}$$

with $\boldsymbol{D}$ being a constant. Using the Gauss theorem, we can show that

$$t^*(\boldsymbol{\xi}) = \int_{\partial\Omega}(\boldsymbol{D}\boldsymbol{x})e^{-i\boldsymbol{\xi}\boldsymbol{x}}ds = \boldsymbol{D}[\boldsymbol{x}\delta]_{\partial\Omega}(\boldsymbol{\xi}) \tag{53}$$

The explicit expression of $(\delta)_{\partial\Omega}(\boldsymbol{\xi})$ for circles and polylines are given in Section 2.6.
To compute the average flux $\boldsymbol{G}$ of the porous material over the domain Ω, we use the average formula

$$\boldsymbol{G} = \frac{1}{\Omega}\int_\Omega k_r\boldsymbol{e}_r d\boldsymbol{x} = \frac{V}{\Omega}k_r\boldsymbol{e}_r(\boldsymbol{\xi} = \boldsymbol{0}) \tag{54}$$

2.6 | Fourier transform of curve based functions

The resolution of the method requires the knowledge of Fourier transform of the boundary functions associated to prescribed flux (33), prescribed temperature (41), and to the computation of $\boldsymbol{e}_r$ from θ_r. They are given in the general form

$$(\boldsymbol{f}\delta)_C(\boldsymbol{\xi}) = \frac{1}{V}\int_C e^{-i\boldsymbol{\xi}\boldsymbol{x}}\,\boldsymbol{f}(\boldsymbol{x})ds \tag{55}$$

where $\boldsymbol{f}(\boldsymbol{x})$ is a function of coordinate $\boldsymbol{x}$ on the curve/surface C. Given the geometry C and function $\boldsymbol{f}$, it is not always possible to derive an analytical formula for $(\boldsymbol{f}\delta)_C(\boldsymbol{\xi})$, except for a limited number of special cases. However, as a numerical method, we can always discretize C into smaller line/planar segments where $\boldsymbol{f}$ is linear or constant, depending on approximation degree. The problem is thus reduced to the calculation of the following functions with properties

$$\text{For } f(\boldsymbol{x}) = 1 \quad (\delta)_C(\boldsymbol{\xi}) = \chi_C(\boldsymbol{\xi}), \quad \text{For } f(\boldsymbol{x}) = \boldsymbol{x} \quad (\boldsymbol{x}\delta)_C(\boldsymbol{\xi}) = -i\frac{d}{d\boldsymbol{\xi}}\chi_C(\boldsymbol{\xi}) \tag{56}$$

and any linear combination of the two above elementary cases.

The analytical expression for line segments is relatively simple. Let us consider a line segment of length $2l$ connecting the two points $\boldsymbol{v}_1$ and $\boldsymbol{v}_2$ where $\boldsymbol{f}$ varies linearly from $\boldsymbol{f}(\boldsymbol{v}_1)$ to $\boldsymbol{f}(\boldsymbol{v}_2)$. By denoting the quantities $\boldsymbol{l}, \boldsymbol{c}$ as

$$\boldsymbol{l} = \frac{1}{2}(\boldsymbol{v}_2 - \boldsymbol{v}_1), \quad \boldsymbol{c} = \frac{1}{2}(\boldsymbol{v}_1 + \boldsymbol{v}_2) \tag{57}$$

we can derive $(\boldsymbol{f}\delta)_{\mathcal{L}}(\boldsymbol{\xi})$ as follows

$$\begin{aligned}
&\text{For } f(\boldsymbol{x}) = 1, \quad (\delta)_C(\boldsymbol{\xi}) = \frac{1}{V}\int_{\boldsymbol{v}_1}^{\boldsymbol{v}_2} e^{-i\boldsymbol{\xi}\boldsymbol{x}} ds = \frac{2l}{V} e^{-i\boldsymbol{\xi}\boldsymbol{c}} \text{sinc}(\boldsymbol{\xi}\boldsymbol{l}) \\
&\text{For } \boldsymbol{f}(\boldsymbol{x}) = \boldsymbol{x}, \quad (\boldsymbol{x}\delta)_C(\boldsymbol{\xi}) = \frac{1}{V}\int_{\boldsymbol{v}_1}^{\boldsymbol{v}_2} \boldsymbol{x} e^{-i\boldsymbol{\xi}\boldsymbol{x}} ds = \frac{2l}{V} e^{-i\boldsymbol{\xi}\boldsymbol{c}} \left[\frac{i\boldsymbol{l}}{(\boldsymbol{\xi}\boldsymbol{l})} [\cos(\boldsymbol{\xi}\boldsymbol{l}) - \text{sinc}(\boldsymbol{\xi}\boldsymbol{l})] + \boldsymbol{c}\,\text{sinc}(\boldsymbol{\xi}\boldsymbol{l}) \right]
\end{aligned} \tag{58}$$

When C is a close circle and $\boldsymbol{f}$ is a local normal vector $\boldsymbol{f} = \boldsymbol{n}$, it is possible to derive the exact expressions for $(\boldsymbol{n}\delta)_C(\boldsymbol{\xi})$. Using the Gauss theorem, we can show the relations

$$(\boldsymbol{n}\delta)_C(\boldsymbol{\xi}) = \frac{1}{V}\int_C \boldsymbol{n}(\boldsymbol{x}) e^{-i\boldsymbol{\xi}\cdot\boldsymbol{x}} ds = -i\boldsymbol{\xi}\chi_C(\boldsymbol{\xi}) \tag{59}$$

where χ is the indicator function of domain inside C, that is, $\chi(\boldsymbol{x}) = 1$ inside C, otherwise $\chi(\boldsymbol{x}) = 0$ and $\chi(\boldsymbol{\xi})$ is the form factor. For a circle of radius R centered at $\boldsymbol{c}$, we have

$$\chi_C(\boldsymbol{\xi}) = \frac{2\pi R^2}{V} \frac{J_1(\eta)}{\eta} e^{-i\boldsymbol{\xi}\boldsymbol{c}}, \quad \eta = R\sqrt{\xi_1^2 + \xi_2^2} \tag{60}$$

where J_1 is the Bessel function of the first kind and first order. In the case where C is a planar (2D) shape in 3D space, analytical expression for form factors $\chi_C(\boldsymbol{\xi})$ of plane polygons are well documented in the literature of scattering physics.[30] Denoting the normal vector to the plane of a given polygon as $\boldsymbol{n}$ and its J vertex as $\boldsymbol{v}_1, \boldsymbol{v}_2, \ldots, \boldsymbol{v}_J$ in counterclockwise direction with respect to $\boldsymbol{n}$, $\chi_C(\boldsymbol{\xi})$ admits the simple form

$$\chi_C(\boldsymbol{\xi}) = \frac{1}{V} \frac{2i(\boldsymbol{n}\times\boldsymbol{\xi})}{(|\boldsymbol{\xi}|^2 - (\boldsymbol{\xi}\boldsymbol{n})^2)} \sum_{j=1}^{J} \boldsymbol{l}_j \text{sinc}\left(\boldsymbol{\xi}\boldsymbol{l}_j\right) e^{-i\boldsymbol{\xi}\boldsymbol{c}_j} \tag{61}$$

with

$$\boldsymbol{c}_j = \frac{1}{2}(\boldsymbol{v}_j + \boldsymbol{v}_{j-1}), \quad \boldsymbol{l}_j = \frac{1}{2}(\boldsymbol{v}_j - \boldsymbol{v}_{j-1}), \quad \boldsymbol{v}_0 \equiv \boldsymbol{v}_J \tag{62}$$

The analytical calculation for $(\boldsymbol{x}\delta)_C(\boldsymbol{\xi})$ as derivative of $(\delta)_C(\boldsymbol{\xi})$ by (56) is not difficult but more cumbersome. A detailed consideration of 3D simulations based on the above formulation will be addressed in future works. To examine the performance of the method, we shall focus on 2D configurations where curve based functions are used.

2.7 | Reconstruction of physical fields from solutions in Fourier space

After solving the LS equation by the iteration method presented in this work, we obtain the solution in wavevector space $\theta_r(\boldsymbol{\xi})$. Due to the finite resolution, the inverse DFT will yield the values $\theta_r(\boldsymbol{x})$ in physical space

$$\theta_r(\boldsymbol{x}) = \text{DFT}^{-1}[\theta_r(\boldsymbol{\xi})] \tag{63}$$

at the grid points only. In practice, we are also interested in values at locations which can be arbitrary. To this end, we use the property of the delta function. The delta function at $\boldsymbol{x}_0$ has the Fourier transform expression

$$\delta_{\boldsymbol{x}_0}(\boldsymbol{\xi}) = e^{-i\boldsymbol{\xi}\boldsymbol{x}_0} \tag{64}$$

The real value $\theta_r(\boldsymbol{x}_0)$ at an interior point $\boldsymbol{x}_0$ where θ_r is continuous is given by the expression

$$\theta(\boldsymbol{x}_0) = \theta_r(\boldsymbol{x}_0) = \frac{1}{V}\int_V \delta_{\boldsymbol{x}_0}(\boldsymbol{x})\theta_r(\boldsymbol{x}) d\boldsymbol{x} = \sum_{\boldsymbol{\xi}} \delta_{\boldsymbol{x}_0}(\boldsymbol{\xi})\theta_r(-\boldsymbol{\xi}) \tag{65}$$

As mentioned, the above relation is valid when θ_r is continuous in $\boldsymbol{x}_0$. There are cases when the points of interest lie on the smooth discontinuity surface $\partial\Omega$ or Γ. For example, if we want to determine the temperature θ on the boundary from the skeleton solution θ_r which vanishes in the void, we can write

$$\theta(\boldsymbol{x}_0) = 2\theta_r(\boldsymbol{x}_0) = \frac{2}{V}\int_V \delta_{\boldsymbol{x}_0}(\boldsymbol{x})\theta_r(\boldsymbol{x})d\boldsymbol{x}, \quad \boldsymbol{x}_0 \in \Gamma, \partial\Omega \tag{66}$$

In another special case where the point $\boldsymbol{x}_0$ belongs to the non-smooth 2D corner of a discontinuity surface, for example, corner with angle γ of a 2D polygon, the factor $2\pi/\gamma$ must be used in the formula (Figure 2)

$$\theta(\boldsymbol{x}_0) = \frac{2\pi}{\gamma}\theta_r(\boldsymbol{x}_0) = \frac{2\pi}{\gamma V}\int_V \delta_{\boldsymbol{x}_0}(\boldsymbol{x})\theta_r(\boldsymbol{x})d\boldsymbol{x}, \quad \boldsymbol{x}_0 \in \text{corner} \tag{67}$$

This relation is due to the symmetry of the delta function at the point of interest $\boldsymbol{x}_0$. In 2D, it can be considered as the limit of a spike function with circle base shrinking to $\boldsymbol{x}_0$. Compared to the full $\delta_{\boldsymbol{x}_0}\theta$ involving the full circle, that is, angle 2π, the integral $\delta_{\boldsymbol{x}_0}\theta_r$ only involves a fraction of the circle, corresponding to the corner angle γ. It is also interesting to note that the treatment of the factor $2\pi/\gamma$ at the corner of the present method is similar to the one used in boundary integral equation (BIE). The two previous cases can be included in the last formula as $\gamma = 2\pi$ (interior point) and $\gamma = \pi$ (smooth boundary).

2.8 | Relation to the BIE

At this stage, we have seen that the present method shares numerous common points with the method of BIE. Now, we shall show, starting from the governing equation, that our method is fundamentally related to BIE. Indeed, taking (30) with $\boldsymbol{E} = 0$ and $k_0 = k_r$ as a special case, we find that

$$\theta_r = \Theta_r + \frac{1}{k_0}S * s + 2\boldsymbol{R} * (\boldsymbol{n}\delta)_{\Gamma_r}\theta_r \tag{68}$$

As mentioned above, θ_r at any point on the boundary is connected to θ via the relation $\theta = 2\pi/\gamma\theta_r$ and $\theta = 2\theta_r$ for the most part of the boundary Γ_r. The difference at some non-smooth corners where $\gamma \neq \pi$ on Γ_r, does not affect the whole integral with $\boldsymbol{R}$ on the right-hand side of (68). Thus, it is safe to write

$$\frac{\gamma}{2\pi}\theta = \Theta_r + \frac{1}{k_0}S * s + \boldsymbol{R} * (\boldsymbol{n}\delta)_{\Gamma_r}\theta \tag{69}$$

By construction of S and $\boldsymbol{R}$ in (4) and their roles in (20), we conclude that S/k_0 is the periodic Green function acting on the source term s and $\boldsymbol{R} = \nabla S$. Substituting s with flux on the boundary and writing the above expression in real space yield the equation

$$\frac{\gamma(\boldsymbol{x})}{2\pi}\theta(\boldsymbol{x}) = \Theta_r - \frac{1}{k_0}\int_{\partial\Omega\cup\Gamma_r} S(\boldsymbol{x}-\boldsymbol{y})j_n(\boldsymbol{y})d\boldsymbol{y} + \int_{\partial\Omega\cup\Gamma_r}\frac{\partial S}{\partial n}(\boldsymbol{x}-\boldsymbol{y})\theta(\boldsymbol{y})d\boldsymbol{y} \tag{70}$$

It is now clear that after some manipulation, we found an interesting form that is similar to the classical BIE formulation. However, in the classical BIE, the Green function for infinite media appears in the governing equation. In

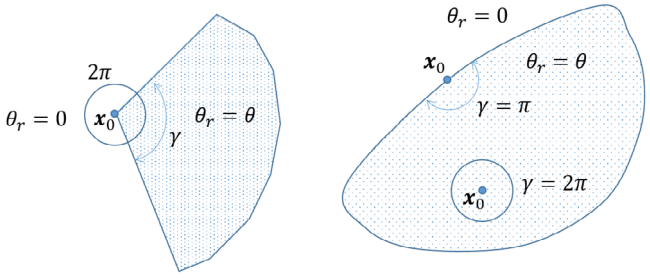

FIGURE 2 Illustration of angle γ for $\boldsymbol{x}_0$ at the non-smooth corner, on a smooth boundary, and inside the skeleton domain

our case, the V-periodic Green function is used and the boundary equation contains the additional constant Θ_r. The origin of the latter constant is due to the periodicity condition and to the fact that the Green function S is defined for a zero average temperature field generated by a unit heat source. Letting the domain become infinitely large $V \to \infty$, S will become the Green function of the infinite media, $\Theta_r \to 0$ and we will recover the original BIE. The present method also relies on the reference conductivity k_0 and it is only when $k_0 = k_r$ that we recover an equation that looks like the usual BIE. Finally, the iterative scheme coupled with FFT, makes the present method rather different from BIE.

2.9 | General BC and pixel/voxel images

As shown previously, the formulation can be used to deal with general boundary value problems in porous material: Neumann (Section 2.4), mixed Dirichlet–Neumann (Section 2.5) BC, including the homogeneous boundary flux and gradient as particular cases. The periodicity BC can be naturally combined by not adding extra void space along the periodic direction. The boundary geometry and the variation of prescribed temperature and normal flux on the boundary can be arbitrary, being described by using a piecewise linear approximation (Section 2.6).

The present method can be applied to any microstructure obtained from pixel/voxel images. Digital image processing algorithms[31] are used to detect the boundary cells which are then linked to construct boundary lines/faces.[21] Depending on how we define the cell connectivity, from 4 to 8-connectivity, the final results may vary. For 4-connectivity, the adjacent cells must share an edge and the line elements are parallel to the plane x_1, x_2, x_3 (see Figure 3). For 8-connectivity, the adjacent cells are only required to have a common corner and consequently horizontal, vertical, and diagonal lines are available. In our experiences, the latter option results in a reduced number of cell points, corners and yields better approximations of the smooth geometries. However, it still introduces artifacts at corners with limited number of angle values, which generates singularities and fluctuations of fluxes near these locations (see the example in Section 3). Hence, only flux results sufficiently far from the boundary are reliable. Further improvements to minimize the corner effects can be proposed, for example, by averaging coordinates of neighboring cells or spline approximations, and so forth, which will be under consideration.

3 | NUMERICAL EXAMPLES

3.1 | Conduction in a periodic structure with heat sources

We shall examine first the performance of the method when dealing with periodic problems with a source term. As an example, we consider an array of solid cylinders surrounded by a fluid and the 2D conduction problem in the plane normal to the cylinders. Such a problem can be used for applications in heat exchanger systems. The conductivity of fluid and solid are respectively $k_f = 1$ and $k_s > k_f$. We vary the value of k_s for the parametric study. It is worthwhile noticing that in this first application, the inclusions are solid and the exterior medium is fluid, contrarily to the case of porous medium studied thereafter.

For simplicity, no macroscopic temperature gradient and heat flux are present $\boldsymbol{E} = \boldsymbol{0}$ and $\boldsymbol{J} = \boldsymbol{0}$. The unit cell is a square domain of dimension $L_1 = L_2 = 1$ and the radius of the cylinder is $R = 0.2$. The cylinders act as heat sources and the fluid

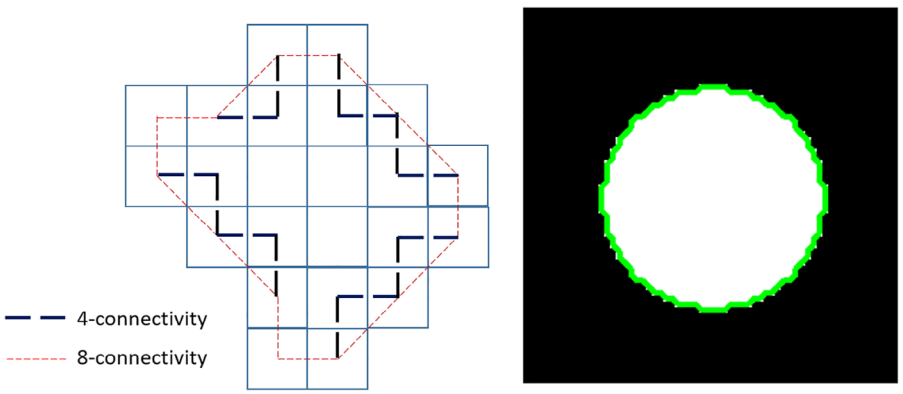

FIGURE 3 Left: Tracing boundary from pixel images using 4 and 8-connectivity. Right: Boundary pixel of circles

as heat sink with homogeneous source terms in each domain

$$s(\boldsymbol{x}) = s_f = 1/(1-f) \quad \text{in the fluid domain,}$$
$$s(\boldsymbol{x}) = s_s = -1/f \quad \text{in the solid domain} \tag{71}$$

with f being the volume fraction of the cylinder $f = \pi R^2/(L_1 L_2)$. These two values ensure the average $\langle s(\boldsymbol{x})\rangle = 0$. The energy exchange rate between the cylinder and the fluid is thus equal to unity

$$q = |s_f|(1-f)V = |s_s|fV = 1, \quad V = L_1 L_2 = 1 \tag{72}$$

We define the heat transfer coefficient as

$$h = \frac{q}{|\theta_f - \theta_s|} = \frac{1}{|\theta_f - \theta_s|} \tag{73}$$

where θ_f and θ_s is the average temperature of the fluid and solid phase.

We use the FFT based schemes presented in Section 2.2 to solve our problem in a sufficiently large domain of wave vectors. In this case, the number of wavevectors $\boldsymbol{\xi}$ defined by (2) is bounded by the inequality $-N \leq n_i \leq N$ with $i = 1, 2$ and $N = 128$. The solution from the FFT based method will be compared with the finite element method (FEM). We use the transient heat transfer module in COMSOL, a standard FEM code, for this purpose. Due to the symmetry, the boundary of the FEM model is of insulation type (zero heat flux). Starting from the initial homogeneous zero temperature, the system temperature evolves to a stable temperature, where we stop to record the result.

Figure 4 shows the result for the case $k_s = 10$. The gradient value along direction 1 and on axis x_1 issued from the FFT based method is in good agreement with the FEM solution. The FFT based scheme converges after a moderate number of iterations (8, 17, and 50 iterations for j, τ, and e schemes) for the accuracy of $\varepsilon = 10^{-3}$. The difference between the minimal and the maximal temperatures is found identical for both cases $\theta_{\max} - \theta_{\min} = 0.1369$. The difference between the temperatures of the fluid and of the cylinder is also identical and equal to $|\theta_f - \theta_s| = 0.091547$. The effective heat transfer coefficient is $h_{eff} = 10.923$ for both methods.

We remark that all the schemes, $\boldsymbol{e}, \boldsymbol{j}$, and $\boldsymbol{\tau}$, yield the same results. These schemes differ only by the convergence rate. The latter depends on the contrast ratio k_s/k_f, the microstructure, the driving force s and $\boldsymbol{E}$ (or $\boldsymbol{J}$ or $\boldsymbol{T}$). To study this, we vary the contrast ratio by varying the conductivity k_s. Figure 5 shows the convergence rate of the three schemes. We find that with the source term, the $\boldsymbol{e}$ and $\boldsymbol{\tau}$ schemes show the same behavior for both high and small contrast. In the log-log plot, they both exhibit symmetry with respect to the origin $|\log k_s/k_f| = 0$ and are linear starting from the ratio $|\log k_s/k_f| \geq 1$. The slope of $\boldsymbol{\tau}$ scheme is about two times smaller than the one of $\boldsymbol{e}$ scheme, meaning that $\boldsymbol{\tau}$ scheme is faster. This behavior is also observed in the homogenization problem without source term, that is, $\boldsymbol{E}, \boldsymbol{J}, \boldsymbol{T} \neq 0$ and $s = 0$. The main difference comes from the $\boldsymbol{j}$ scheme. While the convergence rate of $\boldsymbol{j}$ scheme is similar to the one of $\boldsymbol{e}$ scheme at small contrast ratio $k_s/k_f < 1$, it is superior to the two other schemes at high contrast ratio $k_s/k_f > 1$. Investigation into very high contrast range, up to $k_s/k_f = 10^6$ shows (right part of Figure 5) that the number of iterations to reach convergence appears to be stable at 36 iterations for the $\boldsymbol{j}$ scheme. This interesting issue related to the superconductive limit $k_s = \infty$ suggests that

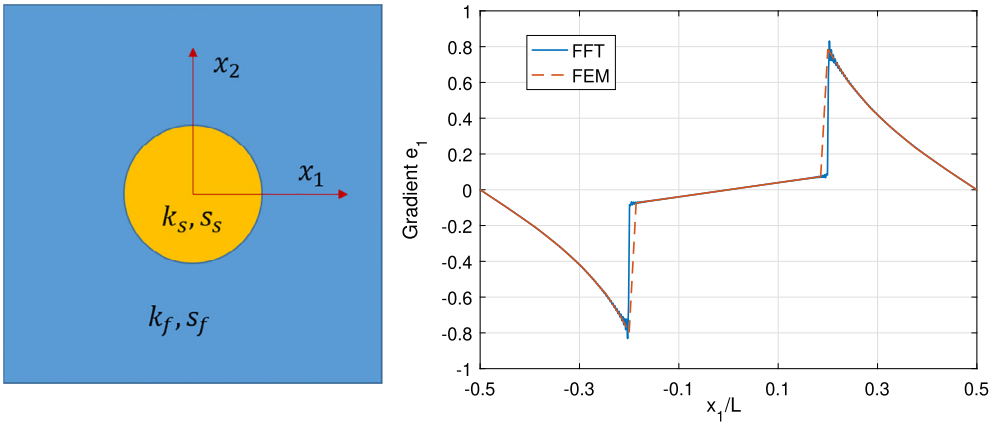

FIGURE 4 Sketch of the periodic heat transfer problem and the obtained results (FEM and FFT methods) for gradient component e_1 on axe x_1

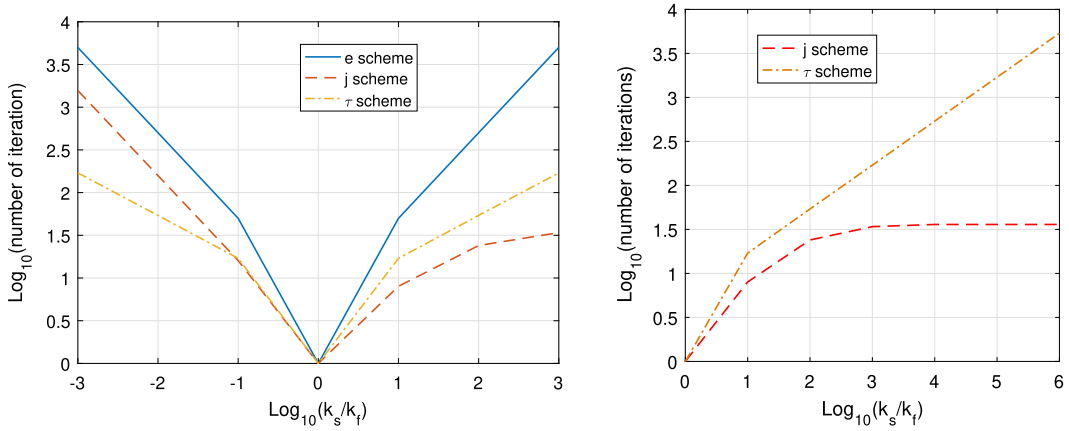

FIGURE 5 Influence of the contrast ratio k_s/k_f on the convergence of iteration schemes

only ***j*** scheme can work in this case. Considering the other extreme limit $k_s = 0$ which is the focus of this article, we find that all schemes fail to converge in this extreme situation. From a physical point of view, this can be explained by the fact that the flux induced by heat sources can be transmitted to the fluid by the superconducting medium, but not by an insulating medium. We will see thereafter that the problem with boundary sources at the boundary of a voided inclusion can be used accurately by the scheme devoted to porous materials described in the previous section.

3.2 | Hollow cylinder subject to flux and temperature BC

In this part, we shall apply the FT method developed in the previous sections to 2D homogenization problems. The same resolution parameter $N = 128$ and tolerance $\varepsilon = 10^{-3}$ as in the previous periodic examples are used. The skeleton of the porous material has a conductivity k_r and the reference conductivity is chosen as $k_0 = 1.2k_r$ to achieve the optimal convergence. It should be also noted that to guarantee the accuracy, the delta terms associated to the boundary $(\boldsymbol{n}\delta)_{\Gamma_r}$ and $(\boldsymbol{n}\delta)_{\partial\Omega\cup\Gamma_r}$ standing before the convolution $*$ in Algorithms 3–5 need to use a higher resolution $\alpha_d N$ than the base resolution N of the unknown θ_r. As suggested in Reference 21, we take $\alpha_d = 2$ in the examples.

We consider first the case of a circular hollow cylinder limited by two circles of radius $R_1 = 0.2$ and $R_2 = 0.4$. The internal boundary is free of flux and the external boundary is subject to homogeneous heat flux along direction 1 with unit intensity $\boldsymbol{G} = \boldsymbol{i}_1$. Since the analytical solution exists for this problem (see Appendix B), it is interesting to compare it with the present method. With the procedure described in Section 2.3, the iteration scheme is stopped after 59 iterations. The effective analytical value of conductivity $k_e = 0.6$ compares well with $k_e = 0.6028$ (FFT). Qualitatively, we find that the temperature θ_r and gradient e_{r1} fields in Figure 6 vanish in the void space and change gradually along direction 1 of the prescribed flux $\boldsymbol{G}$. To study the accuracy of the local solution, we need to examine the distribution of temperature more quantitatively. Considering the variation of those quantities on the axis x_1 (see Figure 7), we find that the temperature profile is antisymmetric and that e_{r1} is symmetric while vanishing in the pore. Near the interface, we observe strong oscillations due to the Gibbs phenomenon as expected. In the polar coordinate system, we fix the radius $r = 0.2$ (internal boundary), $r = 0.4$ (external boundary), and $r = 0.3$ (middle layer) while the polar angle ϕ is varied. To recover the temperature value θ from θ_r at those points, we need to use the results in Section 2.6 and the corresponding factors $2\pi/\gamma$: 2 ($\gamma = \pi$) for the two boundaries $r = 0.4$ and $r = 0.2$ and 1 ($\gamma = 2\pi$) for interior layer $r = 0.3$. In the numerical solution, the temperature varies as a cosinus function of the angular coordinate ϕ, is maximal at $\phi = 0$, and vanishes at $\phi = \pi/2$, which matches perfectly with the analytical solution, for $r = 0.2, 0.3$ and 0.4.

Next, we consider the case of a square hollow cylinder limited by two squares of sides 0.4 and 0.8 subject to homogeneous gradient $\boldsymbol{D} = \boldsymbol{i}_1$ condition along direction 1, that is, $\theta = \boldsymbol{D}\boldsymbol{x} = x_1$ on the external squared boundary. As expected in Figure 8, the temperature increases from the minimal value -0.4 in the left to the maximal value 0.4 in the right. The effective conductivity 0.5800 (FFT) compares well with $k_e = 0.5815$ (FEM). Like for the case of the hollow cylinder, we extract the temperature from the two boundaries and the middle layer to compare with the FEM solutions. Those points lie on the squares of side $2a$ and $a = 0.2, 0.3, 0.4$. The corresponding factors $2\pi/\gamma$ described in Section 2.6 are the

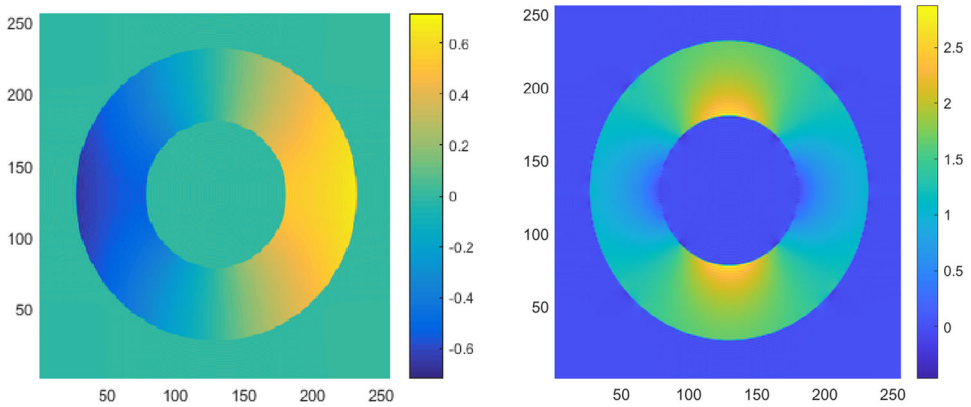

FIGURE 6 Temperature θ_r and gradients e_{r1} field produced by FFT method

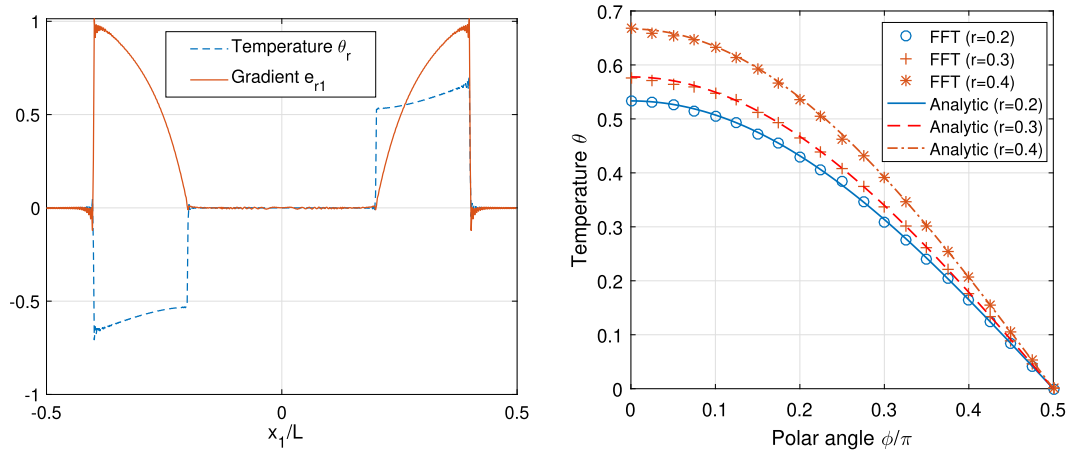

FIGURE 7 Left: Temperature θ_r and gradient e_{r1} along the axis x_1. Right: Temperature θ_r along the circumferential direction in comparison with the analytical solution in Appendix B

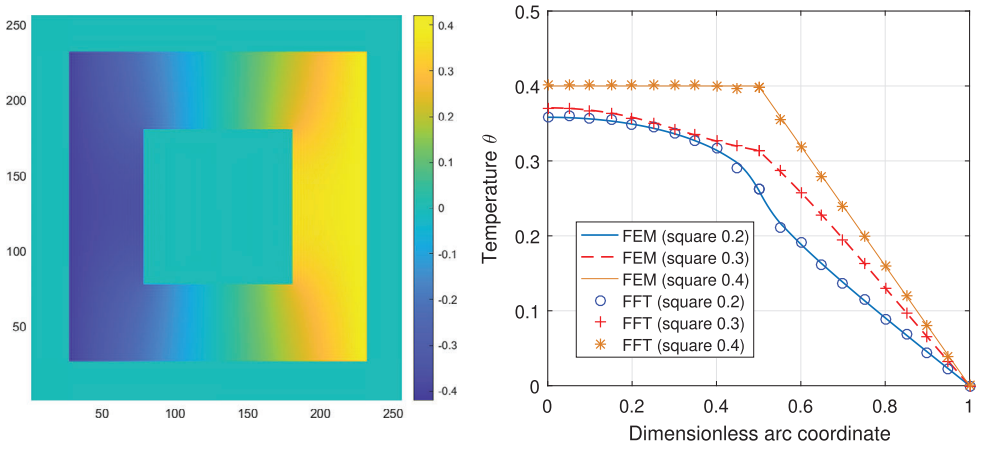

FIGURE 8 Temperature field produced by FFT method and comparison with FEM solution on polylines parallel to the boundary

following: 2 ($\gamma = \pi$) for the two boundaries $a = 0.4$ and $a = 0.2$ except at corners and 1 ($\gamma = 2\pi$) for interior layer $r = 0.2$. Regarding corners, the factors $2\pi/\gamma$ take the following values: 4 ($\gamma = \pi/2$) for the interior corner of the boundary $a = 0.4$ and $4/3$ ($\gamma = 3\pi/2$) for the interior corner of the boundary $a = 0.2$. From Figure 8, we find that the temperature values are well imposed on the external boundary $a = 0.4$, constant and equal to 0.4 on the face $x_1 = 0.4$ and vary linearly on the face $x_2 = 0.4$. The FFT and FEM results are also in excellent agreement for the layers $a = 0.2$ and $a = 0.3$ as well. Combined with the example of circular ring, this confirms at the same time the accuracy of the newly developed FFT algorithm for porous media and the techniques of reconstructing temperature values at arbitrary points using delta function.

The iteration schemes established in Section 2.5 are considerably slower than the one for a pure flux BC. The required number of iterations in both schemes is of order 10^5 iterations. It can also be seen that the augmented Lagrange scheme performs better than the penalty scheme (with $k_{pen} = 10^4$) in terms of imposing temperature constraint. From Figure 9, we can observe how the flux divergence and temperature BC errors decrease with the number of iterations. The two errors have a similar trend in the augmented Lagrangian method. They both decrease fast at the beginning and slower at the end. In contrast, the convergence on the flux divergence of the penalty method is slow at the beginning and fast near the end. Because the penalty coefficient is equivalent to interface conductivity in imperfect interface model, the temperature is stabilized and ceases to evolve after the value obtained at convergence, which is slightly different from the prescribed temperature. In principle, we can increase the penalty coefficient to improve the accuracy of the scheme at convergence. However, this action is comparable to an increasing of contrast ratio in the original FFT schemes and will penalize further the performance of the method.

3.3 | Periodic porous plate subject to mixed BC

We have shown that the FT method can be applied to nonperiodic boundary value problems. Given the performance of the FT method with both periodic and nonperiodic BC, we shall study a porous wall with mixed BC. The wall can be modeled as a domain with finite thickness 0.8 along direction 2 and being periodic along direction 1 with period 1. The random sequential adsorption method is used to generate randomly 15 circular pores of radius 0.06 and a porosity 0.212 in the domain. To avoid percolation issues, that is, circles touching each other and the boundaries, we control a minimal gap of 0.02.

First, we apply a homogeneous flux of intensity 1 along direction 2 on the two surfaces. After 67 iterations, the scheme converges and yields the effective conductivity $k_{e2} = 0.6432$, which compares well with the Maxwell estimate for an isotropic material giving 0.6502. From the field of j_2 in Figure 10, we can observe the interaction between neighboring pores by the strong flux intensity flowing through the gap between them. Looking at the surface temperature θ, we find that the distribution is not homogeneous with peaks and troughs. It is interesting to note the three peaks in the absolute temperature profiles $|\theta|$ corresponding to three circle locations near the boundary. Peaks are more pronounced for holes which are nearer to the wall.

Next, we study the problem using the temperature BC. The uniform temperature distribution θ is prescribed on the two surfaces with value 0.4 and -0.4 and the temperature field shown in Figure 11 shows the gradual change for two locations. The augmented Lagrange scheme converges after 3430 iterations and yields the effective conductivity $k_{e2} = 0.6436$, which is close to the value obtained by the previous example. Regarding the surface flux profile, we find that it is not uniform. The locations of maxima appear to be at the gap between the pore and the minimum at the center of the pore near the surfaces. We conclude that the physical aspects of the heat transfer phenomena are also well recovered in this case.

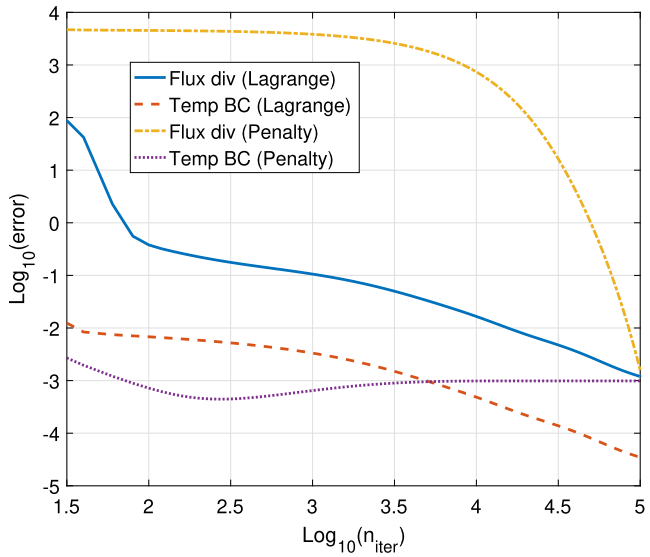

FIGURE 9 Evolution of errors in penalty scheme ($k_{pen} = 10^4$) and augmented Lagrange scheme

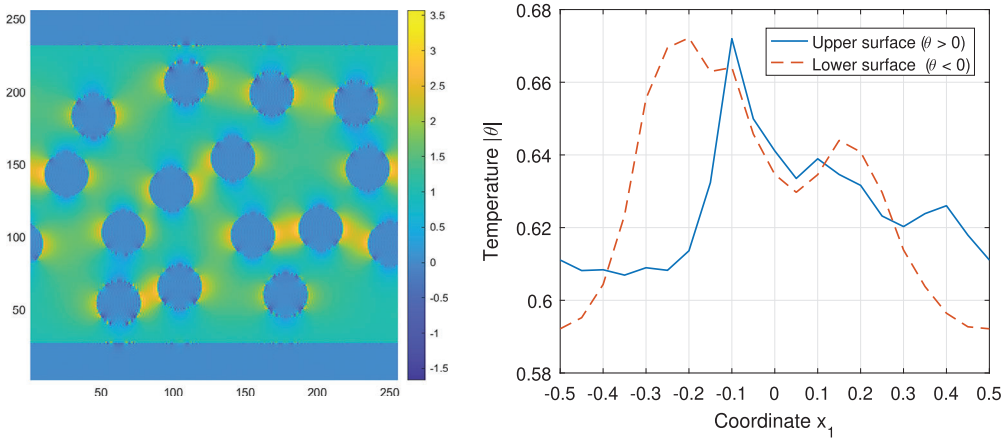

FIGURE 10 Flux field j_2 obtained by FFT method and variation of temperature θ on the surface

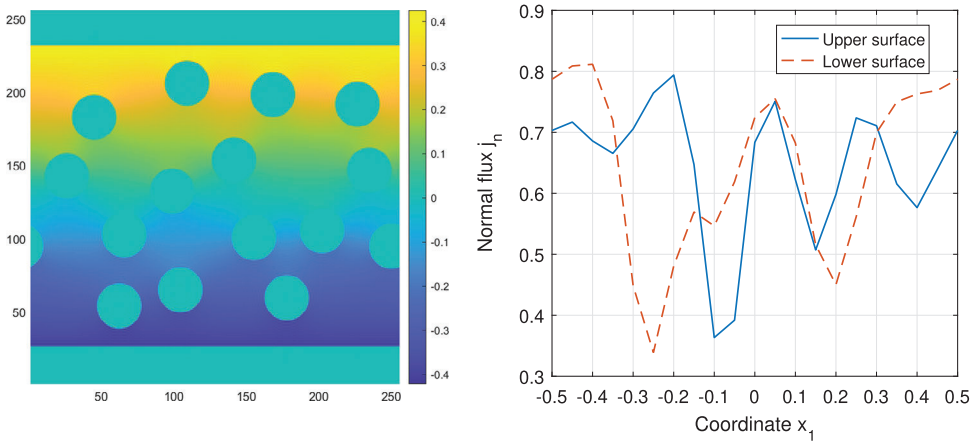

FIGURE 11 Temperature field θ_r obtained by FFT method and variation of normal flux j_2 on the surface

Up to now, the description of phases has been effected by using form factors. However, the FFT method is particularly interesting for images obtained from a pixelized description. So, in the last example, we compare both methods of description. We consider a periodic plate with a sinusoidal boundary and interior holes with heterogeneous BCs. The two boundaries are defined by the equations $x_2 = 0.4 + 0.02\cos(2\pi x_1)$ and $x_2 = -0.4 - 0.02\cos(2\pi x_1)$. The hole is located at the origin with radius $R = 0.2$. The upper plate boundary is subject to Neumann BCs $j_n = 1 + 0.2\cos(2\pi x_1)$ and the lower boundary subject to Dirichlet BCs $\theta = 0.1\cos 2\pi x_1$. The hole boundary is subject to Neumann BCs $j_n = 1$. To solve this problem, the plate upper and lower boundaries are discretized into 20 line elements. Regarding the hole boundary, we use two types of discretization for comparison purpose. In the first model, the circle is discretized with 20 line elements and in the second model the 8 connectivity pixel based boundary of the circle is used (see Section 2.9). Results in Figure 12 (two top subfigures) show that both models yield similar temperature fields. The main differences can be found in the flux field j_2 (see two bottom subfigures of Figure 12). While the two models yield globally the same results, the local values near the pixel based boundary contain strong fluctuations. The maximal absolute flux in the pixel model is 5–6 times higher than the linearized boundary model. These "singularities" can be explained by the artificial corners generated by the pixel images. In contrast, the use of linearized boundary makes the boundary almost smooth and thus avoids those corner effects.

3.4 | Influence of the choice of volume V

From the setting of the method, we only require that the domain under consideration Ω is embedded in a larger volume V without specifying its size. This is based on the fact that any function defined on a finite interval can be expressed by using Fourier series with larger periods. Although the solution of the problem is independent from the period V, the accuracy of the Fourier series, the convergence rate of the numerical schemes may be sensitive to this choice. For example, choosing

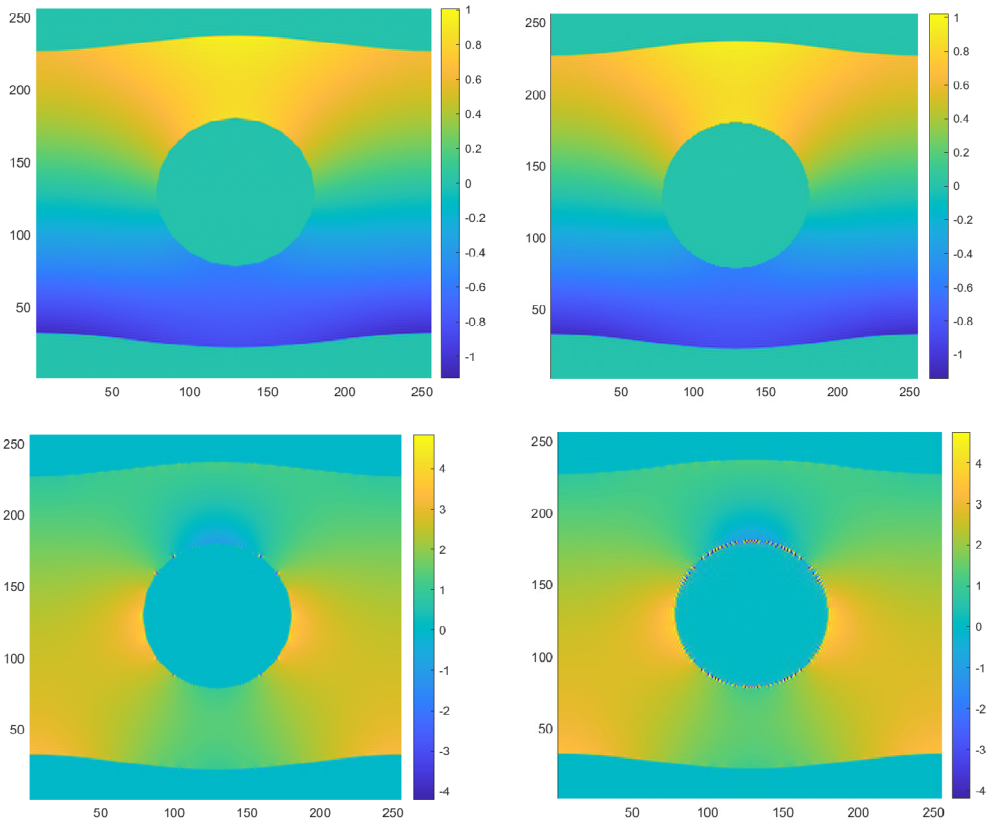

FIGURE 12 Top: Temperature fields θ_r obtained by FFT methods using linearized boundary (left) and pixel based boundary (right). Bottom: Flux components j_2 obtained by FFT methods using linearized boundary (left) and pixel based boundary (right)

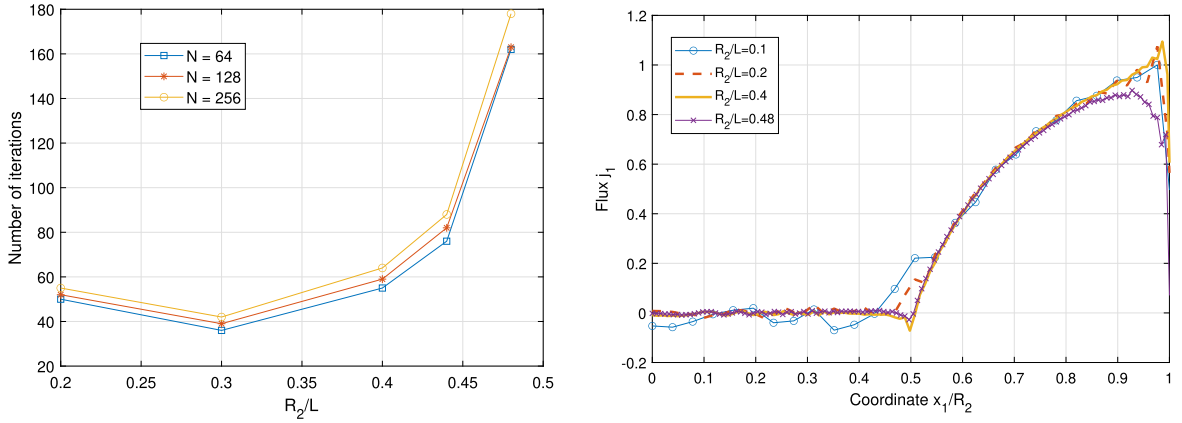

FIGURE 13 Left: Influence of the period V on the number of iterations. Right: Influence of the period V on the result j_2 at resolution $N = 64$

V too large may lead to need a higher resolution N and therefore a higher computation cost. Choosing V which fits tightly to Ω, also requires a finer resolution due to the space between V and Ω and more iterations because we are approaching the extreme case where V touches Ω, violating the periodicity condition imposed on θ_r.

To demonstrate the above arguments, we take the example of a hollow cylinder in Section 3.2. The ratio $R_2/R_1 = 2$ is kept fixed while the resolution N is varied from 64 to 256 and the relative size of the volume R_2/L from 0.1 to 0.48 (here V touches Ω at $R_2/L = 0.5$). From Figure 13, we find that the number of iterations is less sensitive to the resolution parameters N and more sensitive to the period parameters R_2/L. After reaching the optimal number of iterations at $R_2/L = 0.3$ (around 40 iterations), it increases rapidly with R_2/L, especially the smallest period case $R_2/L = 0.48$. To examine the accuracy of the results, let us take the lowest resolution $N = 64$. When we look at the flux j_2 on the axis of symmetry $x_2 = 0$, we find that the results are rather stable between $R_2/L = 0.2$ and $R_2/L = 0.4$. Stronger deviations from the stable profiles are observed at larger and smaller period L. For a large period $R_2/L = 0.1$, a large deviation is observed in the void

space and for small period $R_2/L = 0.48$, the deviation is in the skeleton phase, especially at locations near the boundary of V. However, what is interesting is that despite these local fields, the effective conductivities k_e for all cases are all situated around the exact value 0.6, except for the extreme case $R_2/L = 0.48$ and lowest resolution $N = 64$ which yields the effective value $k_e = 0.58$. The relative errors of all the remaining cases are less than 0.2%. This confirms that the FFT method is a satisfying numerical homogenization method.

4 | CONCLUSIONS

In this article, we have presented an extension of the FFT based method, used mainly up to now for solving problems with periodic BC, in order to solve boundary value problems involving conductive porous media. All types of BC including Neumann, Dirichlet, periodicity (and combination of these conditions) which are frequently used in homogenization procedure can be treated by the method. The ingredient of the method is the integral equation of LS type for periodic porous materials and the associated iteration scheme. Unlike the conventional LS equations for heterogeneous materials which solve the whole field and encounter convergence issues at the pore limit, that is, infinite contrast case, the new LS integral equation solves fields in the skeleton phase only and converges fast.

We find that the nonperiodic problems can be solved using periodic LS equations for porous materials with a source term at the boundary and an extension into the outer space along the lines of immersed boundary methods.[27-29] Specifically, the latter can be treated in the same way as the pores and the fluxes on the boundary by using localized source terms. Different examples are considered, demonstrating at the same time the accuracy of the local fields and effective properties and the convergence performance.

DATA AVAILABILITY STATEMENT

The data that support the findings of this study are available from the corresponding author upon reasonable request.

REFERENCES

1. Brown WF Jr. Solid mixture permittivities. *J Chem Phys*. 1955;23(8):1514-1517.
2. Kröner E. Bounds for effective elastic moduli of disordered materials. *J Mech Phys Solids*. 1977;25(2):137-155.
3. Moulinec H, Suquet P. A fast numerical method for computing the linear and nonlinear mechanical properties of composites. *C R Acad II*. 1994;318(11):1417-1423.
4. Michel J, Moulinec H, Suquet P. Effective properties of composite materials with periodic microstructure: a computational approach. *Comput Methods Appl Mech Eng*. 1999;172(1):109-143.
5. Nguyen TK, Monchiet V, Bonnet G. A Fourier based numerical method for computing the dynamic permeability of periodic porous media. *Eur J Mech B Fluids*. 2013;37:90-98.
6. Michel J, Moulinec H, Suquet P. A computational scheme for linear and non-linear composites with arbitrary phase contrast. *Int J Numer Methods Eng*. 2001;52(1-2):139-160.
7. Šmilauer V, Bažant ZP. Identification of viscoelastic CSH behavior in mature cement paste by FFT-based homogenization method. *Cem Concr Res*. 2010;40(2):197-207.
8. De Geus T, Vondřejc J, Zeman J, Peerlings R, Geers M. Finite strain FFT-based non-linear solvers made simple. *Comput Meth Appl Mech Eng*. 2017;318:412-430.
9. Eyre DJ, Milton GW. A fast numerical scheme for computing the response of composites using grid refinement. *Eur Phys J Appl Phys*. 1999;6(01):41-47.
10. Monchiet V, Bonnet G. A polarization-based fast numerical method for computing the effective conductivity of composites. *Int J Heat Fluid Flow*. 2013;23(7):1256-1271.
11. Brisard S, Dormieux L. FFT-based methods for the mechanics of composites: a general variational framework. *Comput Mater Sci*. 2010;49(3):663-671.
12. Brisard S, Dormieux L. Combining Galerkin approximation techniques with the principle of Hashin and Shtrikman to derive a new FFT-based numerical method for the homogenization of composites. *Comput Meth Appl Mech Eng*. 2012;217:197-212.
13. Vondřejc J, Zeman J, Marek I. An FFT-based Galerkin method for homogenization of periodic media. *Comput Math Appl*. 2014;68(3):156-173.
14. Zeman J, Vondrejc J, Novak J, Marek I. Accelerating a FFT-based solver for numerical homogenization of periodic media by conjugate gradients. *J Comput Phys*. 2010;229:8065-8071.

15. Schneider M. On the Barzilai-Borwein basic scheme in FFT-based computational homogenization. *Int J Numer Methods Eng*. 2019;118:482-494.
16. Wicht D, Schneider M, Böhlke T. On Quasi-Newton methods in fast Fourier transform-based micromechanics. *Int J Numer Methods Eng*. 2020. https://doi.org/10.1002/nme.6283.
17. Kabel M, Böhlke T, Schneider M. Efficient fixed point and Newton–Krylov solvers for FFT-based homogenization of elasticity at large deformations. *Comput Mech*. 2014;54(6):1497-1514.
18. Willot F, Abdallah B, Pellegrini YP. Fourier-based schemes with modified Green operator for computing the electrical response of heterogeneous media with accurate local fields. *Int J Numer Meth Eng*. 2014;98(7):518-533.
19. Moulinec H, Silva F. Comparison of three accelerated FFT-based schemes for computing the mechanical response of composite materials. *Int J Numer Methods Eng*. 2014;97(13):960-985.
20. Schneider M, Wicht D, Bohlke T. On polarization-based schemes for the FFT-based computational homogenization of inelastic materials. *Comput Mech*. 2019;64(4):1073-1095.
21. To QD, Bonnet G. FFT based numerical homogenization method for porous conductive materials. *Comput Meth Appl Mech Eng*. 2020;368:113160.
22. Chen Y, Gelebart L, Chateau C, Bornert M, Sauder C, King A. Analysis of the damage initiation in a SiC/SiC composite tube from a direct comparison between large-scale numerical simulation and synchrotron X-ray micro-computed tomography. *Int J Solids Struct*. 2019;161:111-126.
23. Gelebart L. A modified FFT-based solver for the mechanical simulation of heterogeneous materials with Dirichlet boundary conditions. *C R Mecanique*. 2020;348(8-9):693-704.
24. Colombeau JF. *New Generalized Functions and Multiplication of Distributions*. Amsterdam, The Netherlands: Elsevier; 2000.
25. Oberguggenberger M. *Multiplication of Distributions and Applications to Partial Differential Equations. No. 259*. London, England: Longman Scientific & Technical; 1992.
26. Peskin CS. Flow patterns around heart valves: a numerical method. *J Comput Phys*. 1972;10(2):252-271.
27. LeVeque RJ, Li Z. The immersed interface method for elliptic equations with discontinuous coefficients and singular sources. *SIAM J Numer Anal*. 1994;31(4):1019-1044.
28. Li Z. A fast iterative algorithm for elliptic interface problems. *SIAM J Numer Anal*. 1998;35(1):230-254.
29. Feng H, Zhao S. FFT-based high order central difference schemes for three-dimensional Poisson's equation with various types of boundary conditions. *J Comput Phys*. 2020;410:109391.
30. Wuttke J. Form factor (Fourier shape transform) of polygon and polyhedron; 2017. arXiv preprint arXiv:1703.00255.
31. Gonzalez RC, Eddins SL, Woods RE. *Digital Image Processing Using MATLAB*. Hoboken, NJ: Prentice Hall; 2004.

APPENDIX A. PROPERTIES OF THE SERIES AT CONVERGENCE

Now taking the $\boldsymbol{e}$ scheme based on Equation (12), we can show that $\boldsymbol{e}^{(n)}$ satisfy $(10)_1$ at each step n, that is,

$$\boldsymbol{Q}(\boldsymbol{\xi})\boldsymbol{e}^{(n)}(\boldsymbol{\xi}) = 0, \quad \text{or} \quad \boldsymbol{\xi} \times \boldsymbol{e}^{(n)} = 0 \tag{A1}$$

The two equations above are equivalent because in Fourier space, $\boldsymbol{Q}(\boldsymbol{\xi})\boldsymbol{e}^{(n)}(\boldsymbol{\xi})$ is the projection of $\boldsymbol{e}^{(n)}(\boldsymbol{\xi})$ on the plane normal to the wave vector direction $\boldsymbol{\xi}$ and thus $\boldsymbol{e}^{(n)}(\boldsymbol{\xi})$ is colinear with $\boldsymbol{\xi}$. At convergence, the difference between two consecutive steps in Fourier space

$$i\boldsymbol{\xi}(\boldsymbol{e}^{(n+1)}(\boldsymbol{\xi}) - \boldsymbol{e}^{(n)}(\boldsymbol{\xi})) = \frac{1}{k_0} i\boldsymbol{\xi}[\boldsymbol{R}(\boldsymbol{\xi})s(\boldsymbol{\xi}) - \boldsymbol{j}^{(n)}(\boldsymbol{\xi})] \tag{A2}$$

with $\boldsymbol{j}^{(n)}(\boldsymbol{x}) = k(\boldsymbol{x})\boldsymbol{e}^{(n)}(\boldsymbol{x})$, vanishes and thus also guarantees conditions $(10)_2$ on $\boldsymbol{j}^{(n)}$.

Regarding the $\boldsymbol{j}$ scheme based on Equation (13), we can show that at all steps $(10)_2$ verifies

$$\boldsymbol{P}(\boldsymbol{\xi})[\boldsymbol{j}^{(n)}(\boldsymbol{\xi}) - \boldsymbol{R}(\boldsymbol{\xi})s(\boldsymbol{\xi})] = 0, \quad \text{or} \quad i\boldsymbol{\xi}[\boldsymbol{R}(\boldsymbol{\xi})s(\boldsymbol{\xi}) - \boldsymbol{j}^{(n)}(\boldsymbol{\xi})] = 0 \tag{A3}$$

Again $\boldsymbol{P}(\xi)[\boldsymbol{j}^{(n)}(\xi) - \boldsymbol{R}(\xi)s(\xi)]$ is the projection of $\boldsymbol{j}^{(n)}(\xi) - \boldsymbol{R}(\xi)s(\xi)$ on the wave vector direction $\boldsymbol{\xi}$ and thus $\boldsymbol{j}^{(n)}(\xi) - \boldsymbol{R}(\xi)s(\xi)$ is perpendicular to $\boldsymbol{\xi}$. At convergence, the difference between consecutive steps in Fourier space

$$\boldsymbol{j}^{(n+1)}(\xi) - \boldsymbol{j}^{(n)}(\xi) = k_0 \boldsymbol{Q}(\xi)\boldsymbol{e}^{(n)}(\xi) \tag{A4}$$

with $\boldsymbol{e}^{(n)}(\boldsymbol{x}) = \boldsymbol{j}^{(n)}(\boldsymbol{x})/k(\boldsymbol{x})$, vanishes meaning that $(10)_1$ is also satisfied.

Finally, for the $\boldsymbol{\tau}$ scheme based on Equation (15), the difference between consecutive steps in Fourier space can be simplified as

$$\boldsymbol{\tau}^{(n+1)}(\xi) - \boldsymbol{\tau}^{(n)}(\xi) = 2k_0 \boldsymbol{Q}(\xi)\boldsymbol{e}^{(n)}(\xi) - 2[\boldsymbol{P}(\xi)\boldsymbol{j}^{(n)}(\xi) - \boldsymbol{R}(\xi)s(\xi)] \tag{A5}$$

with $\boldsymbol{e}^{(n)}(\boldsymbol{x}) = \boldsymbol{\tau}^{(n)}(\boldsymbol{x})/(k_0 + k(\boldsymbol{x}))$ and $\boldsymbol{j}^{(n)}(\boldsymbol{x}) = \boldsymbol{\tau}^{(n)}(\boldsymbol{x})k(\boldsymbol{x})/(k_0 + k(\boldsymbol{x}))$. As a result, due to the orthogonality of the two operators $\boldsymbol{P}(\xi)$ and $\boldsymbol{Q}(\xi)$, $(10)_{1,2}$ are both satisfied at convergence.

APPENDIX B. ANALYTICAL SOLUTION FOR A HOLLOW CYLINDER

In polar coordinate system (r, ϕ), the flux BC corresponding to $\boldsymbol{G} = G_1 \boldsymbol{i}_1$ can be written as follows

$$j_r(R_2) = G_1 \cos\phi, \quad j_r(R_1) = 0 \tag{B1}$$

The solution for temperature admits the simple form

$$\theta(r, \phi) = \frac{G_1}{k_r}(Ar + Br^{-1})\cos\phi \tag{B2}$$

where A, B are constants

$$A = \frac{R_2^2}{(R_2^2 - R_1^2)}, \quad B = \frac{R_2^2 R_1^2}{(R_2^2 - R_1^2)} \tag{B3}$$

Computing the average gradient D_1 yield the expression

$$D_1 = \frac{1}{\Omega}\int_{\partial\Omega} n_1 \theta ds = \frac{G_1}{k_r}\frac{R_1^2 + R_2^2}{R_2^2 - R_1^2} \tag{B4}$$

and the effective conductivity

$$k_e = \frac{R_2^2 - R_1^2}{R_1^2 + R_2^2}k_r \tag{B5}$$

The numerical application with $R_1 = 0.2$, $R_2 = 0.4$, $G_1 = 1$, $k_r = 1$ shows that

$$A = \frac{4}{3}, \quad B = \frac{0.16}{3}, \quad k_e = 0.6 \tag{B6}$$

The temperature values at $r = 0.2, 0.3$, and 0.4 have the form

$$\theta(0.2, \phi) = \frac{1.6}{3}\cos\phi, \quad \theta(0.3, \phi) = \frac{5.2}{9}\cos\phi, \quad \theta(0.4, \phi) = \frac{2}{3}\cos\phi$$